The Astrophysical Journal, 755:95 (18pp), 2012 August 20 doi:10.1088/0004-637X/755/2/95

EFFECTS OF ROTATIONALLY INDUCED MIXING IN COMPACT BINARY SYSTEMS WITH LOW-MASS SECONDARIES AND IN SINGLE SOLAR-TYPE STARS

E. Chatzopoulos, Edward L. Robinson, and J. Craig Wheeler
Department of Astronomy, University of Texas at Austin, Austin, TX, USA; manolis@astro.as.utexas.edu
Received 2012 March 22; accepted 2012 June 8; published 2012 August 1

ABSTRACT

Many population synthesis and stellar evolution studies have addressed the evolution of close binary systems in which the primary is a compact remnant and the secondary is filling its Roche lobe, thus triggering mass transfer. Although tidal locking is expected in such systems, most studies have neglected the rotationally induced mixing that may occur. Here we study the possible effects of mixing in mass-losing stars for a range of secondary star masses and metallicities. We find that tidal locking can induce rotational mixing prior to contact and thus affect the evolution of the secondary star if the effects of the Spruit–Tayler dynamo are included both for angular momentum and chemical transport. Once contact is made, the effect of mass transfer tends to be more rapid than the evolutionary timescale, so the effects of mixing are no longer directly important, but the mass-transfer strips matter to inner layers that may have been affected by the mixing. These effects are enhanced for secondaries of 1–1.2 $M_{\odot}$ and for lower metallicities. We discuss the possible implications for the paucity of carbon in the secondaries of the cataclysmic variable SS Cyg and the black hole candidate XTE J1118+480 and for the progenitor evolution of Type Ia supernovae. We also address the issue of the origin of blue straggler stars in globular and open clusters. We find that for models that include rotation consistent with that observed for some blue straggler stars, evolution is chemically homogeneous. This leads to tracks in the H-R diagram that are brighter and bluer than the non-rotating main-sequence turn-off point. Rotational mixing could thus be one of the factors that contribute to the formation of blue stragglers.

Key words: binaries: close – blue stragglers – stars: abundances – stars: evolution – stars: rotation – supernovae: individual (Type Ia)

Online-only material: color figures

1. INTRODUCTION

Cataclysmic variables (CVs) have been recognized as binary systems with white dwarf (WD) primaries and studied for decades (Warner 2003). A closely related field, the study of high- and low-mass X-ray binaries (HMXBs and LMXBs, respectively) containing neutron stars and black holes in close binary systems, is somewhat younger, but also mature (Tanaka & Lewin 1995). The general scenario invoked for the low-mass systems includes evolution through a common envelope phase and then subsequent shrinking of the orbit through magnetic braking or emission of gravitational radiation. When the orbit period becomes short enough, hours to days, even unevolved main-sequence (MS) companions can fill their Roche lobes and transfer mass to the compact primaries.

This scenario has been studied quantitatively with stellar evolution and population synthesis codes. The close binary orbits imply that tidal forces should lock the secondary stars into rotational synchronism with the orbital period and the implied rotation can be quite rapid. This synchronization mechanism is efficient for secondaries with convective envelopes. This rapid rotation may, in turn, induce rotational mixing. Rotational mixing in this context has recently been studied by De Mink et al. (2009) and Brott et al. (2011a) in high-mass systems, but most studies of compact binaries with low-mass secondaries have neglected this effect (e.g., Willems & Kolb 2004; Han & Podsiadlowski 2004; Belczynski et al. 2008; Lipunov et al. 2009). Ergma & Antipova (1999) invoke "deep mixing" to account for the apparent hydrogen deficiency of SAX J1808.4-3658, but give no physical model. They note that MXB 1916-05 ($P_{\rm orb}$ = 50 minutes) and MX 1820-30 ($P_{\rm orb}$ = 11.4 minutes) seem to require a Roche lobe filling helium-rich secondary in order to explain its short orbital period (Paczynski & Sienkiewicz 1981).

Carbon deficiency may be another symptom of rotationally induced mixing. Examples of carbon deficient secondaries include the black hole candidate XTE J1118+480, which shows a distinct paucity of carbon since there is no C IV emission detected (Haswell et al. 2002; Gelino et al. 2006) and the black hole X-ray binary A0620-00 in which the C IV doublet is found to be anomalously weak compared to the other lines, consistent with the low carbon abundance deduced from NIR spectra of the secondary star in the system (Froning et al. 2007, 2011). Low-mass carbon deficient secondaries have also been detected in many CV systems. Harrison et al. (2004) concluded that the K dwarf secondary in the CV SS Cyg was deficient in carbon. Bitner et al. (2007) provided estimates for the masses of the secondary star and the WD in SS Cygni ($M_{\rm WD}$ = 0.81 $M_{\odot}$, M_s = 0.55 $M_{\odot}$) and presented a discussion on the unusual evolutionary characteristics of the secondary and Sion et al. (2010) presented an extended analysis of its carbon-poor UV spectrum. Similar behavior has been observed for the CV AE Aqr (Jameson et al. 1980; Eracleous et al. 1994). Harrison et al. (2005) presented more cases of CVs with weak CO absorption lines in their spectra, implying low C abundance, and suggested that material that has been processed through the CNO cycle is finding its way into the photospheres of secondary stars. More systems with close to zero C IV emission were discussed in Gänsicke et al. (2003). In a potentially related context, IbanoğLu et al. (2012) discuss the carbon deficiency in the mass-accreting primaries of Algol systems and attribute it to a carbon deficiency due to CNO burning on the lower-mass, mass-losing secondary.

They do not suggest any specific mechanism for the carbon deficiency of the secondary.

Extensive discussions of the reasons for carbon depletion in the secondaries of CVs are presented in Harrison et al. (2005) and Schenker et al. (2002). As argued in those works, it is possible to greatly deplete carbon by processing it in the massive stars before Roche lobe contact and then stripping off just enough of the outer layers during thermal timescale mass transfer (TTMT) to reveal layers depleted in carbon. The depletion is estimated to be up to a factor of 100 in these models. This may actually happen in some CVs like AE Aqr since there are other reasons for suspecting the secondary in that system is evolved. Nonetheless, there are two problems invoking the mass-stripping mechanism as the only cause of carbon depletion in some CVs. First, it could be that a high fraction of CVs show the carbon anomaly. If so, current population synthesis models cannot account for such a high fraction of higher-mass progenitors (Harrison et al. 2005). Second, the Schenker et al. (2002) mechanism requires fine tuning. The initial stellar masses, orbital periods, and evolutionary stages need to be exactly right at first Roche lobe contact to obtain results that agree with observations.

These issues motivated us to explore the possibility that carbon is depleted by rotationally induced mixing that processes surface material through the core, where it is subjected to partial CN burning. Rotational mixing allows the secondaries to start with lower mass and does not seem to require fine tuning. Sufficient mixing can lead to quasi-homogeneous evolution and perhaps to low-mass helium star secondary stars. This possibility is of general interest, but may be especially interesting in the context of the progenitors of Type Ia supernovae (SNe). Rotationally induced mixing may also be relevant in cases of single stars such as the "blue straggler" stars (BSSs) in open and globular clusters (GCs). Many BSSs are observed to rotate rapidly and to have depleted C/O abundances. Some BSSs may be slow rotators, but as we describe in Section 3.3, some are observed to be rapid rotators. That seems sufficient to mention the possibility of rotationally induced mixing without knowing the origin of the rotation, nor specifically invoking binary tidal locking as the origin of the rotation. We thus also explore the possibility of rotationally induced mixing in BSSs.

As remarked above, rotationally induced mixing in tidally locked massive stars has been investigated in some contexts (de Mink et al. 2009; Brott et al. 2011a). Rotationally induced mixing in massive stars has been investigated in general (Maeder 1987; Maeder & Meynet 2011; Ekström et al. 2008, 2012; Brott et al. 2011b; Yoon et al. 2012), in the context of the progenitors of gamma-ray bursts (GRBs; Heger et al. 2005; Yoon & Langer 2005), and in the context of very massive stars susceptible to the electron/positron pair instability by Chatzopoulos & Wheeler (2012) and by Yoon et al. (2012). Because massive stars tend to be more radiation pressure dominated, they are closer to neutral dynamical stability, and hence, all else being equal, easier to mix. Very low mass stars are thought to be fully convective, and hence to mix spontaneously, but are also so long lived that they do not evolve in the brief history of the Universe. The case that interests us here are stars of modest mass, of order the solar mass. These stars have outer convective, mixing, envelopes, but inner radiative cores that may resist rotationally induced mixing. The issue requires quantitative investigation and that is the subject of this paper.

In Section 2 we describe the stellar evolution models. We present our results in Section 3 and discuss the implications and conclusions in Section 4. The Appendix presents a calibration of rotating, magnetic MESA models with work in the literature.

2. MODELS

We have used the Modules for Stellar Experiments in Astrophysics (MESA version 3647; Paxton et al. 2011) code to calculate the evolution of a grid of low-mass secondaries (0.8 $M_\odot$, 1 $M_\odot$, 1.2 $M_\odot$, 1.5 $M_\odot$, and 1.8 $M_\odot$) for three different metallicities: $Z = Z_\odot$, $Z = 0.1\ Z_\odot$, and $Z = 0.01\ Z_\odot$. Sub-solar metallicity is encountered in the Large and Small Magellanic Clouds (LMC and SMC, respectively) and in GCs and is relevant to CVs and binary systems found there. Models with sub-solar metallicity might also be relevant to Type Ia SN progenitors in other environments. All models were run for two different degrees of zero-age main-sequence (ZAMS) rotation: 0% and 30% of the critical Keplerian rotation $\Omega_{\rm crit} = (g(1-\Gamma)/R)^{1/2}$ where $g = GM/R^2$ is the gravitational acceleration at the surface of the star, G is the gravitational constant, M is the mass, R is the radius of the star, and $\Gamma = L/L_{\rm Ed}$ is the Eddington factor where L and $L_{\rm Ed}$ are the total radiated luminosity and the Eddington luminosity, respectively. Initial (ZAMS) rigid body rotation was assumed in all cases.

The reason we did not consider higher rotational velocities is because for a variety of mass ratios $q = M_2/M_{\rm WD}$ for the binary system, the maximum allowable rotation is about 33%–38% the critical value, where M_2 is the mass of the secondary star and $M_{\rm WD}$ is the mass of the WD. This comes from combining Kepler's third law expressed in terms of angular velocity:

$$\left(\frac{\Omega_{\rm Kep}}{\Omega_{\rm crit}}\right)^2 = (R/a)^3\left(\frac{1+q}{q}\right), \quad (1)$$

with the Paczyński (1971) expression for the Roche lobe radius:

$$(R_L/a) = 0.38 + 0.20\log(q), \quad (2)$$

where $\Omega_{\rm Kep}$ is the Keplerian orbital frequency, R_L is the Roche lobe radius, R is the radius of the secondary star, and a is the orbital separation. Setting $R = R_L$ in Equation (2) to account for the fact that the maximum rotation prior to mass transfer occurs when the secondary fills its Roche lobe, Equations (1) and (2) yield

$$\frac{\Omega_{\rm max}}{\Omega_{\rm crit}} = (0.38 + 0.2\log(q))^{3/2}\left(\frac{1+q}{q}\right)^{1/2}. \quad (3)$$

The dependence on q is weak. For the range $1 < q < 3$ we get $0.33 < \Omega_{\rm max}/\Omega_{\rm crit} < 0.38$. We note that there are binary systems in which the secondaries have smaller rotational periods than the orbital period. Recent examples include some *Kepler* discoveries of binaries consisting of A-type star secondaries and WD primaries (van Kerkwijk et al. 2010; Breton et al. 2012; Carter et al. 2011; Bloemen et al. 2012). We do not consider this possibility here, but the issue of rotational mixing in such systems is clearly of interest.

MESA was run with the Schwarzschild criterion for convection with the fiducial value for the mixing length parameter, $\alpha_{\rm MLT} = 1.5$. Wind-driven mass loss was calculated using the prescriptions of Glebbeek et al. (2009) and de Jager et al. (1988) as implemented in the code. MESA employs a combination of equations of state (EOS), but for the regime of densities and temperatures encountered by low-mass stars, the OPAL EOS

tables of Rogers & Nayfonov (2002) are used. For higher densities and temperatures, the EOS transitions to HELM EOS (Timmes & Swesty 2000). For the treatment of nuclear processes with MESA we employ the "approx21" network (Timmes 1999), which covers all major stellar nuclear reaction rates. The effects of angular momentum and chemical transport via rotation and magnetic fields are treated based on the one-dimensional approximations of Spruit (1999, 2002) and Heger et al. (2000, 2005). Those include different types of mixing due to rotation such as dynamical shear instability, secular shear instability, Solberg–Hoiland instability, Eddington–Sweet (ES) circulation (meridional circulation), Goldreich–Schubert–Fricke (GSF) instability as well as the Spruit–Tayler (ST) dynamo. For the efficiency of rotationally induced mixing, f_c, we adopt the value 0.0228 based on the findings of Brott et al. (2009) who calibrated this parameter using recent observations of massive rotating early B-type stars in the LMC and the SMC. A value of f_c of 0.046 was proposed by Pinsonneault et al. (1989) in order to explain solar lithium abundances while theoretical predictions by Chaboyer & Zahn (1992) provided a value of 0.033, which was adopted in calculations of massive rotating models done by Heger et al. (2000). We note that most of those values are calibrated by observations of rapidly rotating massive nearby stars. There are currently no observations of rapidly rotating (>20%–30% the critical velocity) solar-type stars that can yield a value of f_c directly relevant to them. Rotationally induced mass loss is also calculated following Heger et al. (2000) and is equal to $\dot{M}_{\rm rot} = \dot{M}_{\rm no-rot}/(1 - \Omega/\Omega_{\rm crit})^{0.43}$, where $\dot{M}_{\rm no-rot}$ is the mass loss rate in the case of zero rotation, due to the effect of radiatively driven winds. In order to take into account the inhibiting effect of a gradient in the mean molecular weight in the efficiency of mixing triggered by rotation we adopted the value $f_\mu = 0.1$ which is the same as the one used by Yoon & Langer (2005) who calibrated their models including the effects of ST.

In order to validate the results found with the new MESA stellar evolution code that includes the effects of rotation and magnetic fields against older well-established codes such as the Geneva stellar evolution code (Eggenberger et al. 2008), the Yoon & Langer (2005) code, and the modified KEPLER code introduced by Heger et al. (2005), we ran some of the same models presented in those works with MESA. We present an extensive comparison of the results in the Appendix. There, we also compare our results with observations of nearby massive rotating stars provided by the VLT-FLAMES survey (Hunter et al. 2008, 2009).

In our suite of models, we find that the mixing is dominated by the meridional circulation and the ST mechanism, with the GSF instability having a minor role. The contribution of the ST mechanism tends to be comparable to, or even slightly dominant over, the meridional circulation at mass fraction greater than 0.8–0.9, and to dominate in a shell covering the mass fraction between 0.2 and 0.4. While the basic physics of the ST mechanism is solid, the employment of this complex, multi-dimensional process in a spherical model may be especially suspect. We checked the role of this process by omitting the ST mechanism in a trial calculation of the model with 1.0 $M_\odot$, and $Z = Z_\odot$ rotating at 30% of the critical velocity (see the Appendix, Figure 18). Omission of the ST mechanism changed our results considerably. We find that meridional mixing alone in low-mass stars cannot induce significant surface abundance changes that are adequate to explain the observed features of carbon-deficient binaries. We return to this point in the conclusions.

We define a timescale, $t_{\rm RL}$, as the time for the secondary star to evolve from non-contact to Roche lobe overflow (RLOF). This timescale is ill constrained due to uncertainties involved in the mechanism of angular momentum loss (common envelope evolution, magnetic braking) and can vary over a large range. We will discuss those uncertainties in more detail in Section 3.2. As a fiducial value for the start of RLOF, chosen in order to calibrate our results for different initial masses and present surface abundance ratios at this epoch in Table 1, we choose $t_{\rm RL} \simeq \tau_{\rm MS}$, where $\tau_{\rm MS}$ is the MS lifetime of the secondary. Once our models reach RLOF, a constant mass loss rate typical for CVs can be employed, in the range (2–6) $\times 10^{-10}\,M_\odot$ yr^{-1}. This rate of mass loss reduces the secondary to a mass typically around 0.6 $M_\odot$, characteristic of WD–red dwarf binary systems such as SS Cygni, within $\sim 3 \times 10^9$ yr. This mass loss rate is scaled up by four orders of magnitude if mass loss occurs on a thermal timescale, a scenario that we discuss in Section 4. We emphasize that we consider the evolution of the secondary stars as single stars, and we do not model the evolution of the binary system as a whole. In the case of close binary systems, the secondary stars will experience tidal forces that will change the shape of the star. Rotation will have the additional effect of inducing oblateness. Those effects are not considered in our one-dimensional stellar evolution calculations.

3. RESULTS

3.1. Evolution of Surface Composition

In order to illustrate the general effects of rapid rotation on the evolution of low-mass stars, we present the evolution of $\Omega/\Omega_{\rm crit}$ with time in the left panel and the evolution in the H-R diagram in the right panel of Figure 1 for the 1 $M_\odot$, $Z = Z_\odot$ model. MESA includes solar mixtures on several scales as presented by Asplund et al. (2005). We see that $\Omega/\Omega_{\rm crit}$ slowly increases with time during the MS. This is the result of increasing radius and luminosity and can be shown by considering angular momentum conservation and the definition of $\Omega_{\rm crit}$ as presented in Section 2. Even though $\Omega/\Omega_{\rm crit}$ increases, it remains under the upper limits of 0.33–0.38. As is the case with more massive rotating models, the low-mass rotating stars in the H-R diagram lie everywhere bluer than the evolutionary tracks of the non-rotating stars.

Next, we examine the effect of rapid rotation on the surface abundances of key elements such as ^{1}H, ^{4}He, ^{12}C, and ^{14}N. Sufficient rotational mixing is expected to lead to chemically homogeneous evolution, as observed in more massive stars (Heger et al. 2000; de Mink et al. 2009; Chatzopoulos & Wheeler 2012; Yoon et al. 2012). Mixing of material from the core up to the surface leads to different surface composition than for the non-rotating case. In general, models of rapidly rotating stars are found to be rich in ^{14}N and ^{4}He while heavily depleted in ^{1}H and less so in ^{12}C. Spectroscopy of rapidly rotating massive stars seems to indicate, however, that the efficiency of rotational mixing is still controversial (Hunter et al. 2008; Brott et al. 2011b) since some discrepancies are found with the predictions of some rotating models in the evolution of surface abundances.

Figures 2 through 5 show the evolution of the surface mass fractions of ^{1}H, ^{4}He, ^{12}C, and ^{14}N for the grid of models we investigate in this work. In each figure, the upper left panel shows the results for $Z = Z_\odot$, the upper right panel for $Z = 0.1\ Z_\odot$, and the lower left panel for $Z = 0.01\ Z_\odot$. In all cases solid lines correspond to the $\Omega/\Omega_{\rm crit} = 0$ models and dashed lines to $\Omega/\Omega_{\rm crit} = 0.3$ models. Also, black color denotes $M_2 = 0.8\ M_\odot$, red 1 $M_\odot$, blue 1.2 $M_\odot$, green 1.5 $M_\odot$, and orange

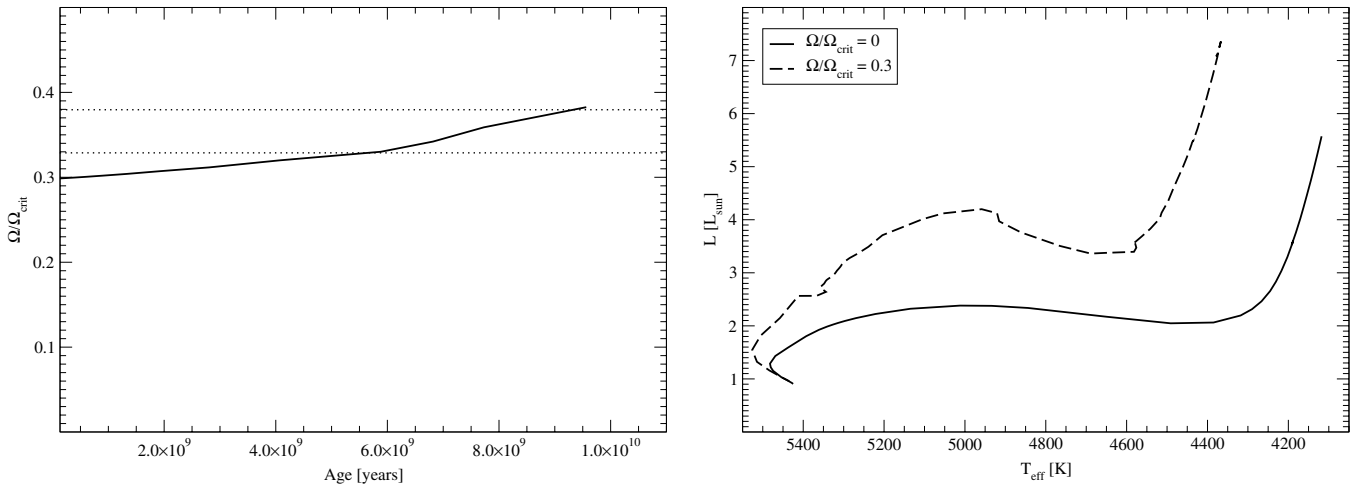

Figure 1. Left panel: evolution of $\Omega/\Omega_{\rm crit}$, during the MS for the 1 $M_{\odot}$, $Z = Z_{\odot}$, $\Omega/\Omega_{\rm crit} = 0.3$ (solid curve) model. The two horizontal vertical lines indicate the range of $\Omega/\Omega_{\rm crit}$ for which the secondary star fills its Roche lobe (see Section 2). Right panel: evolution of the 1 $M_{\odot}$, $Z = Z_{\odot}$, $\Omega/\Omega_{\rm crit} = 0$ (solid curve), and $\Omega/\Omega_{\rm crit} = 0.3$ (dashed curve) models in the H-R diagram.

Table 1
Chemical Properties of the Models for Low-mass Binary Secondaries Studied in this Work

$M_{\rm ZAMS}$ ($M_{\odot}$)	$\Omega/\Omega_{\rm crit,ZAMS}$	$X_{\rm H,s,\tau_{MS}}/X_{\rm H,s,i}$[a]	$X_{\rm He,s,\tau_{MS}}/X_{\rm He,s,i}$[a]	$X_{\rm C,s,\tau_{MS}}/X_{\rm C,s,i}$[a]	$X_{\rm N,s,\tau_{MS}}/X_{\rm N,s,i}$[a]
			$Z = Z_{\odot}$		
0.8	0.0	1.0000	1.0000	1.0000	1.0000
0.8	0.3	0.9640	1.0881	0.8266	1.6979
1.0	0.0	1.0000	1.0000	1.0000	1.0000
1.0	0.3	0.8986	1.1535	0.5018	1.5072
1.2	0.0	1.0000	1.0000	0.8202	1.0000
1.2	0.3	0.9365	1.1520	0.5019	3.5157
1.5	0.0	1.0000	1.0000	0.8202	1.0000
1.5	0.3	0.9698	1.0723	0.5255	3.3124
1.8	0.0	1.0000	1.0000	0.8202	1.0000
1.8	0.3	0.9827	1.0414	0.5574	3.1625
			$Z = 0.1\ Z_{\odot}$		
0.8	0.0	1.0000	1.0000	1.0000	1.0000
0.8	0.3	0.9158	1.2592	0.5754	2.6936
1.0	0.0	1.0000	1.0000	1.0000	1.0000
1.0	0.3	0.9153	1.2653	0.2915	3.7102
1.2	0.0	1.0000	1.0000	1.0000	1.0000
1.2	0.3	0.9101	1.2534	0.1943	4.1908
1.5	0.0	1.0000	1.0000	1.0000	1.0000
1.5	0.3	0.9610	1.1170	0.3182	3.7951
1.8	0.0	1.0000	1.0000	1.0000	1.0000
1.8	0.3	0.9516	1.0995	0.3618	3.2097
			$Z = 0.01\ Z_{\odot}$		
0.8	0.0	1.0000	1.0000	1.0000	1.0000
0.8	0.3	0.8917	1.3472	0.4502	3.2118
1.0	0.0	1.0000	1.0000	1.0000	1.0000
1.0	0.3	0.8363	1.4405	0.0825	5.7059
1.2	0.0	1.0000	1.0000	1.0000	1.0000
1.2	0.3	0.8860	1.3642	0.0687	5.2941
1.5	0.0	1.0000	1.0000	1.0000	1.0000
1.5	0.3	0.8976	1.3049	0.1203	5.4235
1.8	0.0	1.0000	1.0000	1.0000	1.0000
1.8	0.3	0.9254	1.2287	0.1443	5.9529

Note. [a] The ratio of the ZAMS surface mass fraction of a specific element to the surface mass fraction of the same element at the end of the MS.

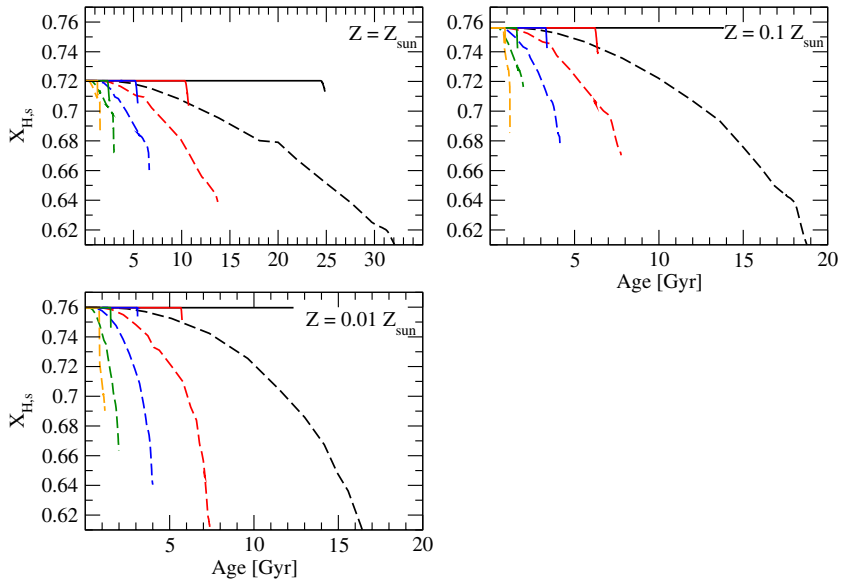

Figure 2. Evolution of the surface hydrogen mass fraction, $X_{\rm H,s}$, for the 0.8 $M_{\odot}$ (black curves), 1 $M_{\odot}$ (red curves), 1.2 $M_{\odot}$ (blue curves), 1.5 $M_{\odot}$ (green curves), and 1.8 $M_{\odot}$ (orange curves) models with $Z = Z_{\odot}$ (upper left panel), $Z = 0.1\ Z_{\odot}$ (upper right panel), and $Z = 0.01\ Z_{\odot}$ (lower left panel). The solid curves are for $\Omega/\Omega_{\rm crit} = 0$ and the dashed curves for $\Omega/\Omega_{\rm crit} = 0.3$. The steep vertical lines for the non-rotating models represent the onset of evolution to the red giant branch, as shown in Figure 6.

(A color version of this figure is available in the online journal.)

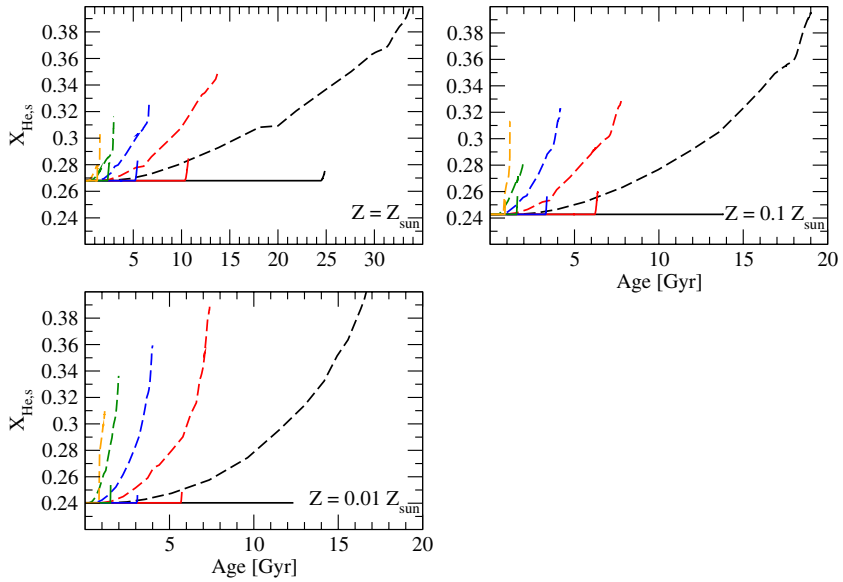

Figure 3. Evolution of the surface helium mass fraction, $X_{\rm He,s}$. The curves represent the same models as those described in the caption of Figure 2.

(A color version of this figure is available in the online journal.)

1.8 $M_{\odot}$. Figure 6 shows the evolution of the stellar radius with time for all the models and also provides information on the MS lifetime of each model before they enter the giant phase. The steep vertical lines for the non-rotating models in Figures 2–5 represent the onset of evolution to the red giant branch, as shown in Figure 6. This transition is muted or modified for the rotating models. Figures 2–6 show that rapidly rotating stars generally live longer than those of zero rotation. All evolutionary tracks have been computed almost up to core helium ignition.

Figure 2 shows the evolution of the surface abundance of hydrogen, $X_{\rm H,s}$, for all the models. The depletion of hydrogen is stronger for intermediate masses and lower metallicities. This is a natural consequence of the fact that somewhat higher-mass stars have hotter interiors so that nuclear burning via the *pp*-chain and CNO cycle processes is more efficient, but as the mass gets even higher, the star lives on the MS for a smaller time that is not sufficient for mixing before it comes in contact or before turning into a giant. The 1 $M_{\odot}$, $Z = 0.01\ Z_{\odot}$, $\Omega/\Omega_{\rm crit} = 0.3$ model reaches $X_{\rm H,s} < 0.62$ by the end of the MS. In Figure 3, the same model is seen to be helium enriched on the surface, compared to the non-rotating case. The outcome of enhanced CNO processing in rotating stars is best seen in Figure 4 where depletion of carbon at the surface occurs toward high rotation, intermediate masses, and lower metallicity and in Figure 5 where the resulting ^{14}N enrichment is seen in the same regions of the parameter space. The results for all models are given in Table 1 where the ratio of surface mass fraction for all those elements on the ZAMS compared to that on the end of the MS is given.

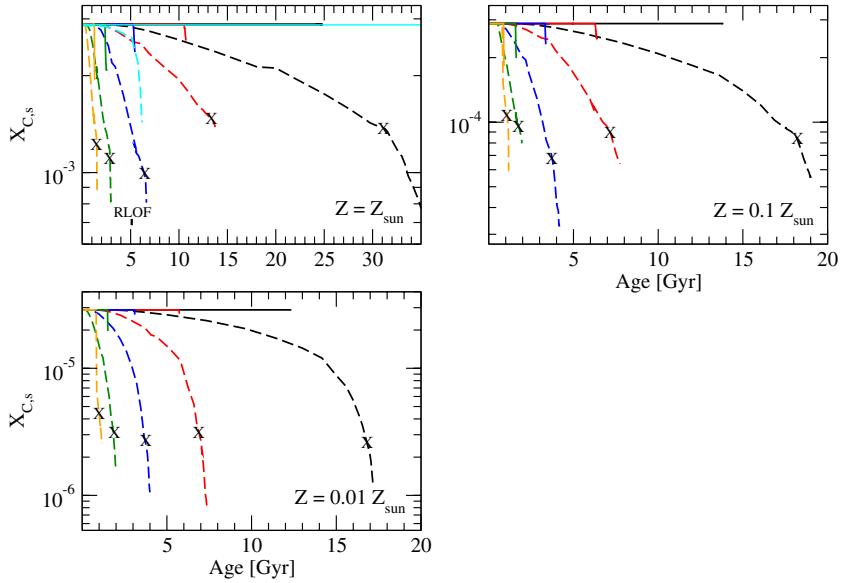

Figure 4. Evolution of the surface carbon mass fraction, $X_{C,s}$. The curves represent the same models as those described in the caption of Figure 2. The light blue curves show the evolution of $X_{C,s}$ for the 1 $M_\odot$, $Z = Z_\odot$, $\Omega/\Omega_{crit} = 0$ (solid), and the 1 $M_\odot$, $Z = Z_\odot$, and $\Omega/\Omega_{crit} = 0.3$ (dashed) models in the case where we adopt an RLOF mass loss rate $\dot{M}_{RLOF} = 5 \times 10^{-10}\, M_\odot\ yr^{-1}$ starting at $t_{RL} = 5 \times 10^9$ yr. The "X" marks indicate the end of the MS for the rotating models. The time of RLOF mass loss is also indicated.

(A color version of this figure is available in the online journal.)

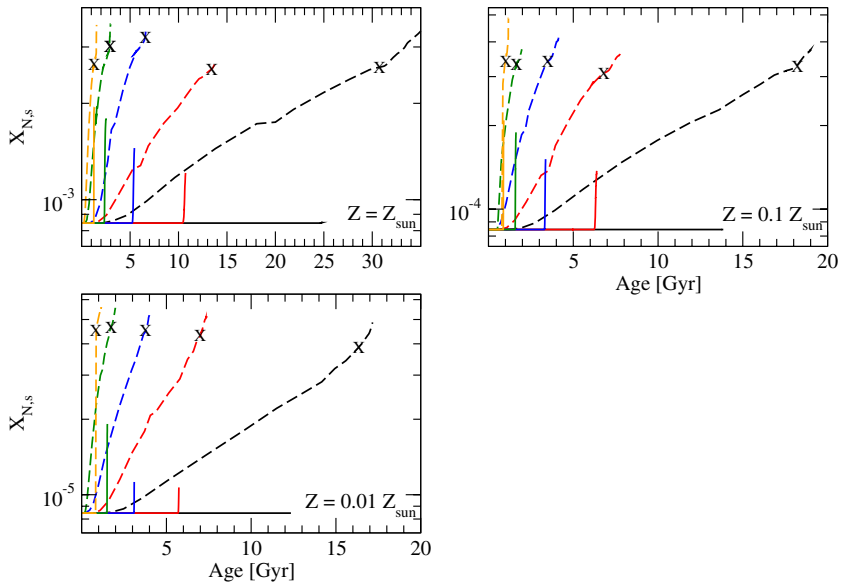

Figure 5. Evolution of the surface nitrogen mass fraction, $X_{N,s}$. The curves represent the same models as those described in the caption of Figure 2.

(A color version of this figure is available in the online journal.)

The effects of rotation on the composition structure of low-mass secondaries are also illustrated in Figure 7. We observe that, even though homogenization is weaker in low-mass stars than it is in more massive stars, the partial mixing that occurs is strong enough to drive abundance changes throughout the interior of the star. This also results in the cores of the rotating stars being somewhat more massive than those of non-rotating ones and in hydrogen depletion at the center being more pronounced, especially for lower metallicities.

In order to investigate the effects of RLOF mass loss on the evolution of the surface abundances of our models, we have run the 1 $M_\odot$, $Z = Z_\odot$, $\Omega/\Omega_{crit} = 0$ and the 1 $M_\odot$, $Z = Z_\odot$, $\Omega/\Omega_{crit} = 0.3$ models up to $t_{RL} \sim 5 \times 10^9$ yr without RLOF mass loss and then turned on a constant mass loss rate of $5 \times 10^{-10}\, M_\odot\ yr^{-1}$, within the range expected for CVs. This mass loss is maintained until the total mass of the star is reduced to $\sim$0.55 $M_\odot$, requiring an interval of $\sim 9 \times 10^8$ yr. The evolution of the surface mass fraction of carbon, $X_{C,s}$, for these models is shown as the solid (non-rotating) and dashed (rotating) light blue curves in the upper left panel of Figure 4. In the case of the non-rotating mass-losing model, $X_{C,s}$ does not change much because carbon depletion is strong only in the inner 0.3 $M_\odot$ of the star and mass stripping does not reach this depth. Also, since we are left with a 0.55 $M_\odot$ star, its MS lifetime is significantly prolonged leaving $X_{C,s}$ at the same value for more than a Hubble time. For the rotating, mass-losing model we see that RLOF mass loss has only a small effect, a decrease of about a factor of two, on the further evolution of the surface carbon abundance. However, the

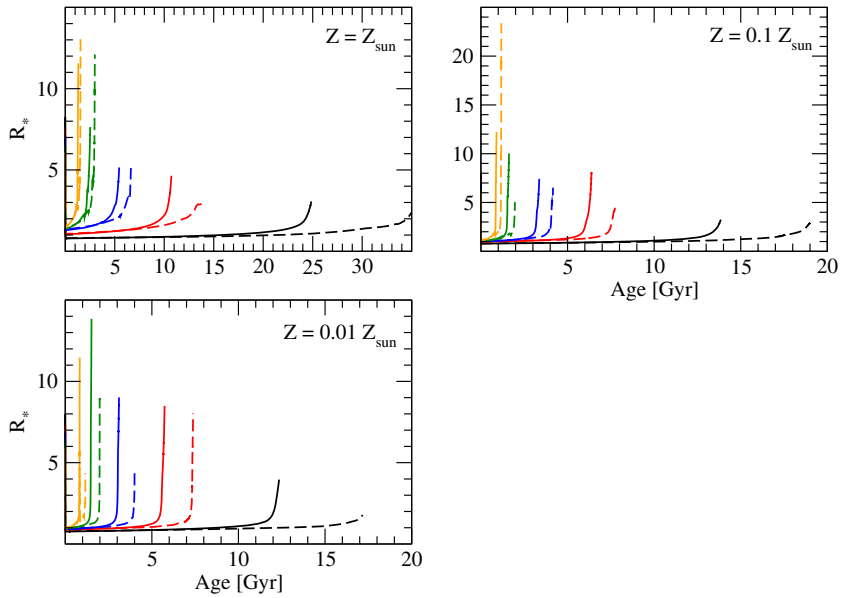

Figure 6. Evolution of the radius of the secondary star, R_*. The curves represent the same models as those described in the caption of Figure 2.

(A color version of this figure is available in the online journal.)

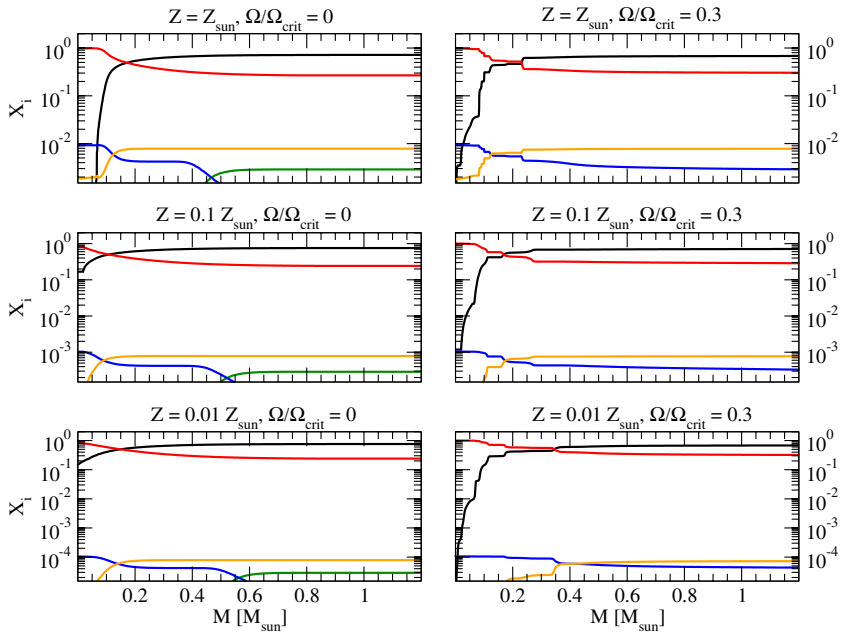

Figure 7. Composition structures of the 1.2 $M_\odot$, $Z = Z_\odot$, $\Omega/\Omega_{\rm crit} = 0$, and $\Omega/\Omega_{\rm crit} = 0.3$ (upper left and upper right panel, respectively) models, the 1.2 $M_\odot$, $Z = 0.1\ Z_\odot$, $\Omega/\Omega_{\rm crit} = 0$, and $\Omega/\Omega_{\rm crit} = 0.3$ (middle left and middle right panel, respectively) models, and the 1.2 $M_\odot$, $Z = 0.01\ Z_\odot$, $\Omega/\Omega_{\rm crit} = 0$, and $\Omega/\Omega_{\rm crit} = 0.3$ (lower left and lower right panel, respectively) models at time $\simeq 3/4\ \tau_{\rm MS}$. In all panels the mass fractions of the following elements are plotted: H (black curves), He (red curves), C (green curves), N (blue curves), and O (orange curves). The discrete steps in the H and He profiles for the rotating models are due to mixing resulting from the rapidly changing magnetic field, and therefore, magnetic viscosity, in these regions.

(A color version of this figure is available in the online journal.)

comparison between the mass-losing non-rotating and rotating models indicates that rotationally induced mixing leading to abundance changes throughout the whole stellar interior remains the main reason for $X_{\rm C,s}$ depletion even when mass loss is accounted for, at least for the fiducial example presented here. It is the mixing that took place the first $\sim 5 \times 10^9$ yr that lead to carbon depletion in the surface as well as in some inner layers in different degrees, with mass loss being a second-order effect because in the absence of such mixing, as can be seen for the non-rotating mass-losing model, mass loss alone did not lead to significant changes. For both mass-losing cases we also note that once the stellar mass becomes small ($<0.8\ M_\odot$), carbon depletion is diminished because the core temperature becomes sufficiently low that the fusion of C to N can no longer take place. In addition, rotationally induced mixing becomes less efficient. In reality, the process of RLOF mass loss is, of course, more complicated and the mass loss rate changes with time such that it starts with initially very high mass loss rate then declines to values characteristic for CVs. We argue that the most interesting phase of chemically quasi-homogeneous evolution in rapidly rotating secondaries is that before, the star loses significant amounts of mass via RLOF. The extent of RLOF mass loss

itself has an impact only on the magnitude of these effects in the sense that deeper regions of the star are probed with somewhat different (but not significantly so) composition.

3.2. Constraints by Loss of Angular Momentum

The effects of rotationally induced mixing on the surface abundances of low-mass secondaries that we presented is Section 3.1 are only valid under the assumption that the secondary star rotates at relatively high velocities (∼30% the critical value) for a sufficient time, $t_{\rm RL}$, before loss of angular momentum causes the secondary to fill its Roche lobe and begin transferring mass to the WD. To investigate the constraints of angular momentum loss on our results we calculate relevant timescales. The timescales we wish to compare are the characteristic timescales for synchronization, for sufficient mixing that leads to considerable surface abundance changes, and for angular momentum loss.

First of all, we demand that the system be synchronized so that the orbital period is equal to the rotational period of the secondary. The synchronization timescale for a binary system based on the influence on tides is given by the following expression (Zahn 1977, 1989):

$$\tau_{\rm sync} = f_{\rm turb}\frac{1}{q^2}\left(\frac{a}{R_2}\right)^6 \ {\rm yr}, \quad (4)$$

where $f_{\rm turb}$ is a constant that depends on the structure of the secondary and is typically of the order of unity for stars with convective envelopes. For a combination of masses and for $a/R_2 \leqslant 20$ the synchronization timescales are less than $\sim 10^8$ yr, indicating that most of the systems under consideration synchronize rapidly compared to their MS life spans. This timescale can be even shorter if radiative dissipation due to oscillation damping near the stellar surface is considered (Zahn 1975). For the mixing timescale, we choose a lower limit of $t_{\rm RL} = 3\times10^9$ yr and an upper limit of $t_{\rm RL} = 7\times10^9$ yr based on the maximum carbon depletion that we find for the representative models of 1 $M_\odot$ and 1.2 $M_\odot$ for $Z = 0.1\ Z_\odot$ and $Z = 0.01\ Z_\odot$ ($X_{\rm C,s}$ declines by about an order of magnitude for these models in the chosen time range).

The angular momentum loss timescale is given by $\tau_{\rm AML} = J/\dot{J}$, where J is the total orbital angular momentum and $\dot{J}$ is the rate of change of the orbital angular momentum. We can write $J = M_\odot^{5/3}G^{2/3}m_{wd}m_2m^{-1/3}\Omega_{\rm orb}^{-1/3}$ with $M_\odot$ the solar mass, G the gravitational constant, m_{wd}, m_2 and m the masses of the WD, the secondary star and the sum of the two in units of the solar mass, respectively (capital letters denote those masses in cgs units), and $\Omega_{\rm orb} = (GM_\odot m/a^3)^{1/2}$ the orbital frequency. The prescription for $\dot{J}$ depends on the angular momentum loss mechanism.

There are two basic models for angular momentum loss in binary systems: angular momentum loss via gravitational radiation (for systems with shorter orbital periods) and via magnetic braking (for systems with larger orbital separation). For angular momentum loss by gravitational radiation Paczyński (1967) gives for $J/\dot{J}$:

$$\tau_{GR} = \frac{1.25\times10^9 r^4}{m_2 m_{wd} m}\left(\frac{a}{R_2}\right)^4 \ {\rm yr}, \quad (5)$$

where $r = R_2/R_\odot$ with R_2 the radius of the secondary star in cm.

Angular momentum loss by magnetic braking was introduced by Verbunt & Zwaan (1981) and is based on the principle that angular momentum is removed from the secondary via magnetically coupled stellar winds. Then, from the orbital tidal synchronization and using their calculated $\dot{J}$ we estimate $\tau_{\rm AML} = \tau_{\rm MB}$ for this process to be

$$\tau_{\rm MB} = \frac{3.33\times10^6 f^2 m_{wd}m_2 r}{k^2 m^3}\left(\frac{a}{R_2}\right)^5 \ {\rm yr}, \quad (6)$$

where f is a constant of order of unity and $k = (0.1)^{1/2}$. Rappaport et al. (1983) offered an updated prescription for angular momentum loss with magnetic braking accounting for the structure of the radiative core and the convective envelope of the secondary. Using their method we calculate

$$\tau_{\rm MB} = \frac{4.38\times10^6 m_{wd}m_2 r^{5-\gamma}}{m^3}\left(\frac{a}{R_2}\right)^5 \ {\rm yr}, \quad (7)$$

where γ is a dimensionless parameter that ranges between 0 and 4. For $\gamma = 4$ an expression close to that of Verbunt & Zwaan (1981) is recovered. To better constrain the magnetic braking mechanism, Sills et al. (2000) obtained rotational data from young open clusters and calibrated the theoretical predictions. They found that the mechanism is less efficient than previously thought. Using Equation (8) for $\dot{J}$ from their work, we derive the corresponding angular momentum loss timescale:

$$\tau_{\rm MB} = \begin{cases} \dfrac{2.88\times10^6 m_{wd}m_2 r^{9/2}}{m^{3/2}}\left(\dfrac{a}{R_2}\right)^5 \ {\rm yr}, & \Omega \leqslant \Omega_X, \\ \dfrac{1.13 m_{wd}m_2 r^{3/2}}{m^{1/2}\Omega_X^2}\left(\dfrac{a}{R_2}\right)^2 \ {\rm yr}, & \Omega > \Omega_X, \end{cases} \quad (8)$$

where $\Omega_X = \Omega_{X,\odot}\tau_{\rm conv,\odot}/\tau_{\rm conv,2}$ is the critical frequency at which the magnetic field apparently saturates (Krishnamurthi et al. 1997), $\tau_{\rm conv,\odot}$ and $\tau_{\rm conv,2}$ are the convective overturn timescales for the Sun and for the secondary star, respectively. Sills et al. (2000) find that a value of $\Omega_X \simeq 10\ \Omega_\odot$ is needed to fit the data, and we adopt the same value in this work. Ivanova & Taam (2003) presented yet another refinement for the angular momentum loss based on the relation between X-ray variability and rotation rate in X-ray binaries. Their relation also has the form of a broken power law and also depends on the magnetic field saturation frequency. Their prescription implies a timescale for angular momentum loss given by the following formula:

$$\tau_{\rm MB} = \begin{cases} \dfrac{3.16\times10^6 m_{wd}m_2 r}{t^{0.5}m^2}\left(\dfrac{a}{R_2}\right)^5 \ {\rm yr}, & \Omega \leqslant \Omega_X, \\ \dfrac{11.35 m_{wd}m_2}{r^{1.55}t^{0.5}m^{1.15}\Omega_X^{1.7}}\left(\dfrac{a}{R_2}\right)^{2.5} \ {\rm yr}, & \Omega > \Omega_X, \end{cases} \quad (9)$$

where $t = T_2/T_\odot$, with T_2 the effective temperature of the secondary and $T_\odot$ the effective temperature of the Sun. In order to calculate the numerical coefficients we have used $\Omega_\odot = 2.9\times10^{-6}$ rad s^{-1}.

The more recent predictions for angular momentum loss by magnetic braking imply a less efficient mechanism than the older predictions. Yet another correction to those laws comes from the fact that stars with a small or no convective mantle do not have a strong magnetic field and will therefore experience little or no magnetic braking (Podsiadlowski et al. 2002; van der Sluys et al.

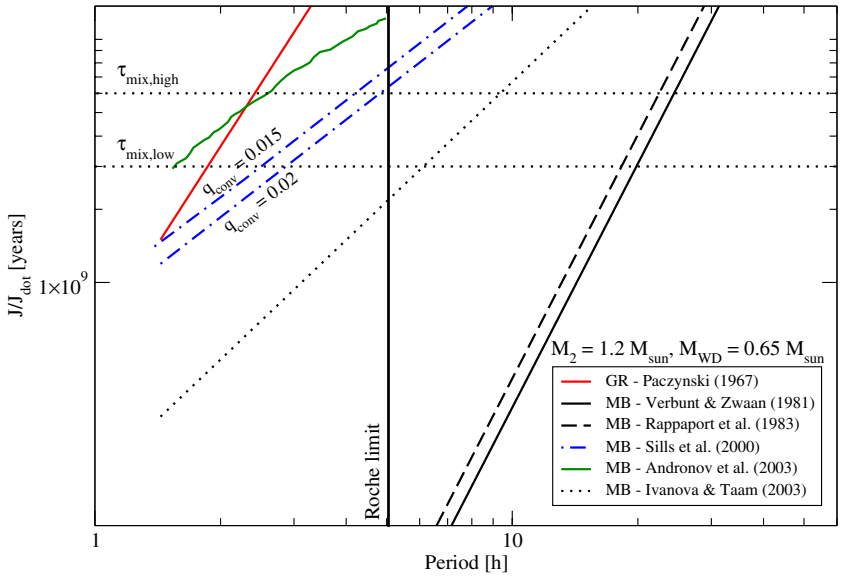

Figure 8. Characteristic timescales for angular momentum loss for a range of orbital periods in the case of a system with a secondary star of mass $M_2 = 1.2\,M_\odot$ and a white dwarf of mass $M_{\rm WD} = 0.65\,M_\odot$, characteristic of SS Cyg. The solid red curve represents the angular momentum loss timescale due to gravitational radiation from Paczyński (1967). The solid and dashed black curves represent $\tau_{\rm MB}$ as calculated by Verbunt & Zwaan (1981) and Rappaport et al. (1983) for $\gamma = 0$, respectively. The dot-dashed blue curves show the longer magnetic braking timescale according to the predictions of Sills et al. (2000) for $q_{\rm conv} = 0.015$ and $q_{\rm conv} = 0.02$. The dotted black curve is based on Ivanova & Taam (2003). The solid green curve is data for the numerically calculated angular momentum loss timescale taken from the upper panel of Figure 4 of Andronov et al. (2003) in the case of an evolved secondary. The horizontal dotted lines indicate the characteristic timescales required for significant rotationally induced mixing to occur based on the results of our evolutionary calculations in Section 3.1. Finally, the solid vertical line indicates the Roche limit expressed in terms of orbital period for this particular system.

(A color version of this figure is available in the online journal.)

2005). In this case, a correction term $\exp(0.02/q_{\rm conv} - 1)$ can be defined, where $q_{\rm conv}$ is the fractional mass of the convective envelope. Adopting this correction to the law of Sills et al. (2000) (Equation (8)) makes the effective angular momentum loss timescale even larger. Large angular momentum loss timescales of the order of a Hubble time due to magnetic braking have also been discussed by Andronov et al. (2003; see Figure 4 of their paper) as well as by Willems et al. (2005). In the context of these long magnetic braking timescales, the period gap for CVs with orbital period between 2 and 3 hr is addressed by invoking two distinct populations. As discussed in Andronov et al. (2003), one population would comprise unevolved secondaries (those with orbital periods of 2 hr or less) and the other evolved secondaries (with orbital periods of 3 hr or more).

The large timescales for magnetic braking posited in the more recent papers imply that it is possible for some close systems to be synchronized and maintain nearly a constant orbital period for long enough that their secondaries rotationally mix, therefore yielding altered surface mass fractions for some elements. To illustrate this idea, we plot all the angular momentum loss timescales discussed above as a function of orbital period in Figures 8 and 9. In Figure 8 we have done so for a system with $M_2 = 1.2\,M_\odot$ and $M_{\rm WD} = 0.65\,M_\odot$, which we suspect is similar to SS Cyg prior to its contact with its Roche lobe. The inset labels the various angular momentum loss timescales for gravitational radiation and magnetic braking. It can be seen that for systems with $P_{\rm orb} \leqslant 7$–8 hr there is sufficient time for the secondary to undergo significant rotationally induced mixing before coming in contact with its Roche lobe, if we accept the recently updated, less efficient magnetic braking laws. In general, for a secondary to sufficiently mix before transferring mass to the WD, a fiducial system has to be in the region between the two dotted lines and toward smaller periods, so that the rotational velocity is higher and therefore the rotationally induced mixing is stronger. In addition, the system has to be below the curves for angular momentum loss as calculated by making use of the latest prescriptions for angular momentum loss via magnetic braking in the same diagram. In Figure 9 we present the same plot, but in the particular case of the system V471 Tau ($M_2 = 0.9\,M_\odot$, $M_{\rm WD} = 0.84\,M_\odot$, $P_{\rm orb} =$ 12.5 hr; O'Brien et al. 2001), which consists of a WD and a red dwarf secondary star. A lower limit for $J/\dot{J}$ in this case was estimated by using the observed $P_{\rm orb}/\dot{P}_{\rm orb}$ coming from the observed minus corrected ($O-C$) diagram. It can be seen that it is possible that this system will mix in the future; however, at that large separation, it probably will not exhibit a significant rotationally induced mixing due to the low orbital frequency.

We conclude that the type of binary system with low-mass secondaries that might undergo significant rotationally induced mixing that leads to enhanced nitrogen and helium and depleted hydrogen and carbon surface abundances is one that evolves in a manner illustrated in Figure 10. Initially (panel (a)), the system consists of a higher-mass primary (M_1) and a lower-mass secondary (M_2). Subsequently, the system undergoes common envelope evolution and the primary dies, becoming a WD, while the secondary is still on the MS (panel (b)). At this point the system is synchronized and the orbital separation is relatively small ($P_{\rm orb} \leqslant 7$–9 hr). The system remains detached and the secondary rotates at high velocities $0.2 \leqslant \Omega/\Omega_{\rm crit} \leqslant 0.33$, thus undergoing rotationally induced mixing (panel (c)). Those fiducial orbital period and corresponding rotational angular velocity limits are implied for significant surface carbon depletion, as shown in Figure 8. The mixing significantly alters the surface element abundances by the end of the MS, leading to the depletion of carbon and the enhancement of nitrogen in the surface. Finally (panel (d)), the system has lost sufficient angular momentum that the secondary comes in contact with its Roche lobe and starts to transfer mass

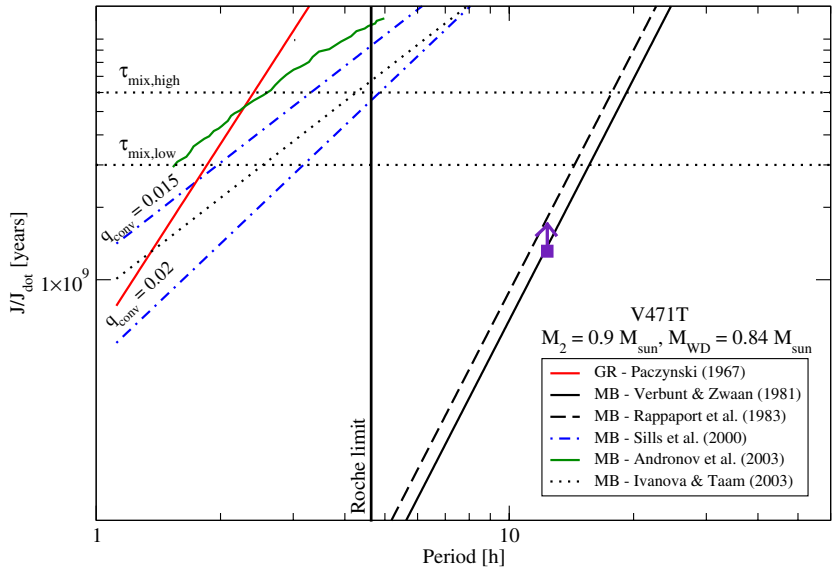

Figure 9. Characteristic timescales for angular momentum loss for a range of orbital periods in the case of a system with a secondary star of mass $M_2 = 1.2\,M_\odot$ and a white dwarf of mass $M_{\rm WD} = 0.65\,M_\odot$, characteristic of the binary V147 Tau (O'Brien et al. 2001; filled purple square). The curves represent the same models as those described in the caption of Figure 8.

(A color version of this figure is available in the online journal.)

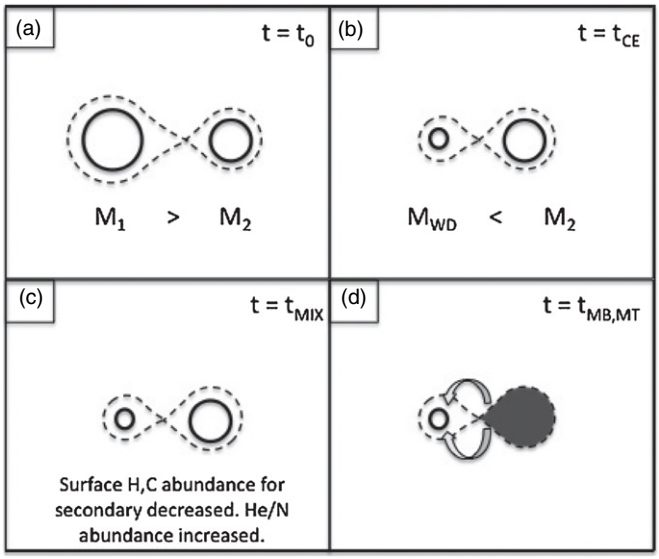

Figure 10. Schematic representation of the evolution of a binary system that leads to reduced surface carbon and hydrogen and enhanced surface helium and nitrogen abundances for the secondary. See the text (Section 3.2) for details.

to the WD. A long timescale between tidal locking and RLOF is consistent with current theories of relatively weak magnetic braking. At the onset of RLOF, unstable mass transfer could occur on the thermal timescale of the secondary or stable mass transfer could ensue for mass ratio $q < 1$ on long timescales characteristic of many CVs, as we have assumed for the model here. The mass transferred to the WD has different abundances from cases where the secondary does not rotate rapidly and thus does not mix enough, or if the secondary fills its Roche lobe before mixing is extensive.

3.3. Application in the Case of Blue Straggler Stars

The inclusion of the effects of rotation in the evolution of solar-type stars may also provide insight to some cases of BSSs first discovered by Sandage (1953) in the GC M3. BSSs are stars in open or globular clusters that appear to be on the MS but are more luminous and bluer than stars at the MS turn-off point in the cluster H-R diagram. BSSs have been found in many globular and open clusters in the Milky Way, notably the globular cluster 47 Tuc (Ferraro et al. 2006), the open cluster NGC 188 (Mathieu & Geller 2009), and the globular cluster M4 (Lovisi et al. 2010).

Suggestions for the origin of BSSs include mass transfer from primordial binaries in low density GCs (MT-BSSs) or even stellar collisions, particularly those that involve binaries (COL-BSSs) in high star density GCs (McCrea 1964; Hills & Day 1976; Fusi Pecci et al. 1992; Ferraro et al. 2003; Davies et al. 2004). There is some evidence that both processes could be active in some clusters (Ferraro et al. 2009). There are still open issues concerning the surface chemical abundances of BSSs. In particular, depleted C/O abundances are associated with BSSs in some clusters, for example in 47 Tuc (Ferraro et al. 2006). In addition, high equatorial velocity has been measured for many BSSs: The equatorial velocity in 47 Tuc is measured to be >10 km s^{-1} (Ferraro et al. 2006), in NGC 188 many BSSs have velocities of up to 50 km s^{-1} (Mathieu & Geller 2009), and in M4 the BSSs equatorial velocities range from 10 km s^{-1} up to 150 km s^{-1} ($\Omega/\Omega_{\rm crit} \sim 0.02$–$0.35$; Lovisi et al. 2010).

The depleted C/O abundances and relatively high rotation that are observed in some BSSs indicate that rotationally induced mixing leading to chemically homogeneous evolution might be relevant for some of those objects. The idea of prolonged strong mixing associated with BSSs was first suggested by Wheeler (1979; see also Saio & Wheeler 1980). With the availability of stellar evolution codes that take into account the effects of rotation, we can attempt to evaluate this hypothesis.

We ran MESA with 1 $M_\odot$ models for solar ($Z = Z_\odot$), 10% solar ($Z = 0.1\,Z_\odot$), and 1% solar ($Z = 0.01\,Z_\odot$) metallicity for four different rotation velocities in the range of those measured for the BSSs in the clusters 47 Tuc, NGC 188, and M4: $v_{\rm rot} =$ 0 km s^{-1}, 10 km s^{-1}, 60 km s^{-1}, and 100 km s^{-1}. The evolution of these models in the H-R diagram is shown in the upper left ($Z = Z_\odot$), the upper right ($Z = 0.1\,Z_\odot$), and the lower left ($Z = 0.01\,Z_\odot$) panels of Figure 10. In all panels, solid curves

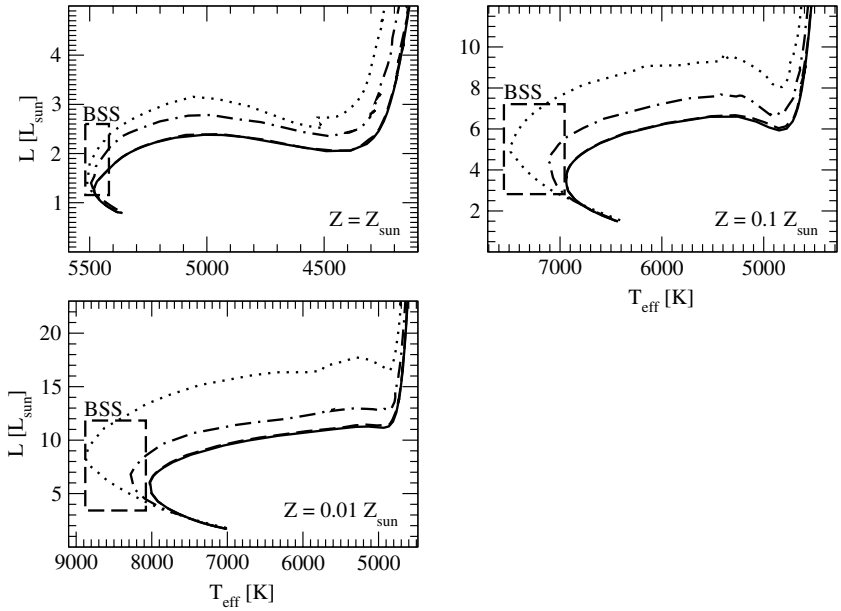

Figure 11. Evolution of blue straggler candidate models on the H-R diagram for 1 $M_{\odot}$, $Z = Z_{\odot}$ (upper left panel), $Z = 0.1\ Z_{\odot}$ (upper right panel), and $Z = 0.01\ Z_{\odot}$ (lower left panel). Solid black curves indicate $v_{\rm rot} = 0$ km s^{-1}, dashed black curves $v_{\rm rot} = 10$ km s^{-1}, dash-dotted black curves $v_{\rm rot} = 60$ km s^{-1}, and dotted curves $v_{\rm rot} = 100$ km s^{-1}. The boxes marked "BSS" indicate where the blue straggler stars are expected to be on the H-R diagram.

represent $v_{\rm rot} = 0$ km s^{-1}, dashed curves $v_{\rm rot} = 10$ km s^{-1}, dash-dotted curves $v_{\rm rot} = 60$ km s^{-1}, and dotted curves $v_{\rm rot} = 100$ km s^{-1}. The "BSS" labeled boxes indicate where BSS candidate stars are expected to be located in the H-R diagram of a cluster. It is evident that the evolutionary tracks of stars with equatorial velocities > 10 km s^{-1} are well within the BSS domain. Given the fact that there is a spread in masses, compositions, and equatorial velocities associated with BSSs we expect that the BSS labeled regions in Figure 11 in reality will be even more densely populated with evolutionary tracks than the sample of models we present here. We conclude that quasi-homogeneous evolution due to rotationally induced mixing may be an alternative, third channel to form BSSs. The rotation to induce the mixing may have arisen in mass-transfer events, so all these mechanisms may be active.

4. DISCUSSION AND CONCLUSIONS

Gänsicke et al. (2003) presented a variety of CVs with very large N_V/C_{IV} flux ratios in far-ultraviolet (FUV) spectra. In the same study it is estimated that 10%–15% of close CVs that have gone through a phase of TTMT show this kind of surface abundance anomalies. Similar cases of large N_V/C_{IV} flux ratios have been observed in some black hole binary systems like XTE J1118+480 (Haswell et al. 2002; Gelino et al. 2006). Most low-mass close binaries are also synchronized and their secondaries are rapidly rotating and therefore evolve quasi-homogeneously due to rotationally induced mixing.

Motivated by these observations, we ran a grid of evolutionary models of low-mass secondaries for different degrees of metallicity and rotational velocity in order to study the effects of rotationally induced mixing in these systems. Vigorous rotationally induced mixing led to a more chemically homogeneous evolution than in non-rotating standard evolution and enabled CNO processing of material in a larger portion of the stellar interior. As a consequence, the hydrogen and carbon surface abundances are reduced and the helium and nitrogen abundances enhanced. This effect is found to be stronger for intermediate mass (1–1.2 $M_{\odot}$), increased rotation, and decreased metallicity for the secondary star. The magnitude of this effect is also bigger for longer timescales after tidal locking and before encountering RLOF mass loss. Once RLOF mass loss starts, the surface abundances do not change significantly and by the time RLOF ends the secondary may be left with low enough mass that the core temperature is not high enough to burn the material that is mixed inward, therefore preventing further homogenization and significant surface abundance changes. Since carbon depletion is more pronounced for higher masses, it is possible that the secondaries of carbon depleted systems were once more massive, even up to 1.2–1.5 $M_{\odot}$, and then lost a significant amount of mass. This can be achieved via a phase of unstable TTMT (Schenker et al. 2002; Podsiadlowski et al. 2003; Gänsicke et al. 2003). In this case, systems with secondaries with mass up to 2 $M_{\odot}$ may subsequently evolve into CVs with low-mass secondaries and slow transfer rates. If the secondary were a fast rotator, the mass transferred will have a high ratio of $X_{\rm N,s}/X_{\rm C,s}$, in agreement with what is spectroscopically observed. Therefore, we conclude that rotationally induced mixing could be one way to explain the carbon-depletion features of some of the systems discussed above.

Altering the abundance of the material accreted onto the WD may affect the subsequent evolution of the WD. Systems containing a WD and a low-mass helium-rich companion are observed (Maxted et al. 2000; Mereghetti et al. 2011). Helium overabundance is spectroscopically observed in some recurrent novae, U Sco (Williams et al. 1981; Hanes 1985; Starrfield et al. 1988) and V394 (Sekiguchi et al. 1989), and some classical novae, Nova LMC 1990 No. 2 (Sekiguchi et al. 1990; Shore et al. 1991) and V445 Puppis (Nova Puppis 2000; Ashok & Banerjee 2003; Kato & Hachisu 2003; Kato et al. 2008; Woudt et al. 2009; Goranskij et al. 2010). In most considerations in the literature, the helium-rich secondaries are the cores of stars stripped of their red giant envelopes by mass transfer (Iben & Tutukov 1994; Yoon & Langer 2003; Solheim & Yungelson 2005; Ruiter et al. 2009, 2011; Wang et al. 2009a, 2009b; Wang & Han 2009; Meng & Yang 2010). Here, we suggest that helium-rich secondaries can arise through rotationally induced

mixing of MS stars. Some of our models exhibit enhanced $X_{\rm He,s}/X_{\rm H,s}$ therefore providing accreting material of a different mixture than has been extensively modeled to date (solar H/He or pure He).

As discussed in Section 2 and in the Appendix, we find interesting levels of rotationally induced mixing only if we include the effects of the ST dynamo on the transport of both angular momentum and chemical abundances. We suspect that rotation, especially differential rotation, will induce magnetic effects and that the omission of magnetic effects is inappropriate. Whether the ST mechanism as employed in shellular models is the "correct" or only magnetic effect is not so clear. Inclusion of the ST mechanism in rotating stellar evolution calculations is "state of the art," and we include it in order to capture some magnetic effects and to compare to other work in the literature that makes comparable assumptions (the Appendix). We emphasize that the inclusion of chemical mixing due to magnetic fields as parameterized by Spruit (2002) is observationally motivated in the present work since it is necessary in order to explain the observed surface abundance changes in some low-mass secondary stars, members of close binaries that are rapid rotators, in the context of stellar evolution with the inclusion of the effects of rotation. The inclusion of magneto-rotational effects in stellar evolution is a topic that surely warrants more attention (Brown et al. 2011).

The inclusion of the effects of rotation in the evolution of some low-mass secondaries may thus have implications for the progenitors of Type Ia SNe. Accretion of hydrogen onto a WD will tend to generate double shell sources that are susceptible to thermonuclear instabilities, including nova explosions. Even with high accretion rates that allow steady hydrogen shell burning, the subsequent helium shell burning is often found to be unstable (Iben & Tutukov 1989; Cassisi et al. 1998; Kato & Hachisu 1999) making it very difficult to construct satisfactory models that grow the WD to near the Chandrasekhar mass, carbon ignition, and thermonuclear explosion. At low accretion rates, the helium shell source in accreting WD models may be thermally unstable even for non-degenerate cases (Cassisi et al. 1998; Langer et al. 2002). Accretion from a hydrogen-poor secondary may modify some of these constraints (Webbink et al. 1987; Truran et al. 1988; Livio & Truran 1992). A higher helium abundance will tend to lead to more stable shell burning. This might alter the conditions of shell burning and hence the constraints necessary for successful Type Ia explosions. Based on our models, the $X_{\rm He,s}/X_{\rm H,s}$ ratio would increase during the accretion process since deeper regions of the rotationally mixed stars become accessible. Further exploration of this issue requires thermonuclear hydrodynamic simulations. We note that although our rotating models linger longer on the MS, the luminosity does increase monotonically. Models that are more helium enriched will thus also tend to be somewhat brighter than ZAMS models of the same mass. All of our models with noticeable helium enrichment are brighter than the upper limit set on a particular SN Ia progenitor system by Schaefer & Pagnotta (2012).

Helium detonations on WDs have also been proposed to be related to the progenitors of the predicted class of subluminous.Ia SNe (Shen et al. 2010). Events such as SN 2002bj (Poznanski et al. 2010) and SN 2010X (Kasliwal et al. 2010) show strong He lines in their spectra, but no sign of H. A potential channel to .Ia progenitors could be one of a close synchronized binary system with a rapidly rotating secondary star that undergoes chemically homogeneous evolution leading to surface He enrichment. Once RLOF mass loss sets in, this He-rich material from the secondary will accrete on the WD and, provided that the accretion rate is appropriate for stable shell burning, it may set the initial conditions appropriate for a .Ia progenitor.

Rotationally induced mixing seems to play a role in the evolution of solar mass rotating single stars as well. As an example we examined the case of BSSs found in many galactic clusters. We found that the inclusion of the effects of rotation in the evolution of solar-type stars might lead some of those with equatorial rotational velocity greater than 10 km s^{-1} to evolve past the MS turn-off point in the H-R diagram. In general, rotation seems to be relevant even in the case of post-MS, yellow supergiant stars (YSGs). Neugent et al. (2012) show that models with rotation agree better with the observed properties of YSGs in the LMC than do models with no rotation.

These results illustrate the importance of rotationally induced mixing leading to chemically quasi-homogeneous evolution of low-mass secondaries in binary systems that are synchronized. Rotationally induced mixing may be fundamental in understanding observational features of some CVs, black hole binaries, or Type Ia SNe and to even some single solar-type stars. This possibility deserves further consideration and modeling.

We thank the MESA team for making this valuable tool readily available and especially thank Bill Paxton for his ready advice and council in running the code. E.C. thanks J. J. Hermes for useful discussions. This research is supported in part by NSF AST-1109801.

APPENDIX

ROTATIONAL MIXING IN MESA: COMPARISON WITH OTHER CODES AND WITH OBSERVATIONS

The effects of rotation in the transport of angular momentum and chemical mixing were only recently implemented in the stellar evolution code MESA (Paxton et al. 2011) that we are using in the present paper. We present here comparisons of MESA with other established codes. Specifically, we focus on the efficiency of the ST mechanism (Spruit 1999, 2002) when the effects of magnetic fields are taken into account. While its precise utility and implementation may be questioned, the effect of the magnetic torques on angular momentum transport as implemented by Spruit is used in many modern stellar evolution codes. The effects of the magnetic field on chemical mixing of elements is even more the subject of debate (Maeder & Meynet 2003, 2004, 2005; Spruit 2006). In some calculations, chemical mixing by the ST mechanism is found to lead to overly efficient mixing and surface N abundances that are higher than those suggested by observations of massive early B-type stars in the Milky Way and in the LMC and SMC (Hunter et al. 2008, 2009). We therefore also focus on assessing the degree to which MESA models with rotation and magnetic fields agree with observations. We stress that this comparison is restricted to massive ($>10\,M_{\odot}$) stars since we are not aware of observations of rapidly rotating solar mass stars and relative N abundance measurements. We note, however, that the findings of the present paper are observationally motivated (depleted carbon abundances in rapidly rotating secondary stars in close binaries) and might constitute the first attempt to compare the effects of rotation and magnetic fields in solar-type stars with direct observations.

The effects of rotation on angular momentum transport (but not chemical mixing), including magnetic torques as parameterized by Spruit, have been included in several stellar evolution

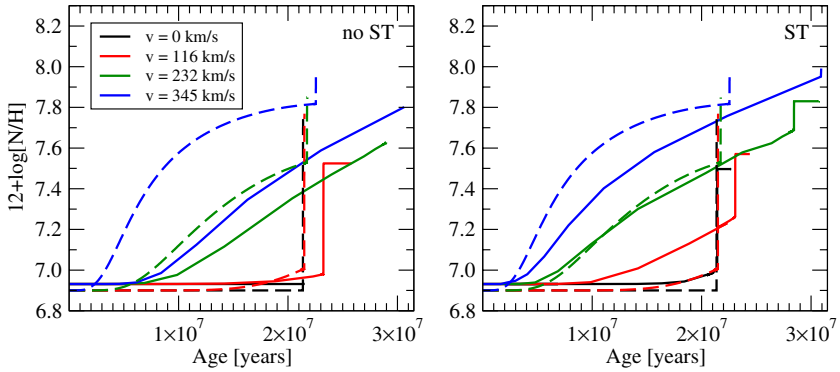

Figure 12. Evolution of surface nitrogen abundance with time for 10 $M_{\odot}$, $Z = 0.0047$ models for ZAMS rotational velocities of 58 (black curve), 116 (red curve), 232 (green curve), and 345 km s^{-1} (blue curve) for a case where the effects of the ST mechanism on chemical mixing are ignored (left panel) and for a case where those effects are included (right panel) as calculated by MESA. Angular momentum transport via the ST mechanism is included in both cases. The dashed curves represent the results from the same models of Brott et al. (2011b).

(A color version of this figure is available in the online journal.)

codes in the past. For the purposes of benchmarking MESA against some of those well-established codes we ran models similar to those presented by Brott et al. (2011a, 2011b), Ekström et al. (2012), Heger et al. (2005), and Yoon et al. (2006, 2012). The models we have selected have been computed by three different stellar evolution codes that include the effects of rotation and, in some cases, magnetic fields: the Geneva code (Eggenberger et al. 2008), the Yoon & Langer (2005) code, and an updated version of the KEPLER code (Weaver et al. 1978) that was first used by Heger et al. (2005) to study progenitors of GRBs. The majority of the models computed in these works are for massive stars. Therefore, most of our comparisons are for massive stars with the exception of solar mass models computed in the grid of Ekström et al. (2012). For all models run with MESA, the same parameters (initial mass and metallicity, ZAMS rotational velocity, mixing, and angular momentum transport efficiency) have been adopted as in the models with which we compare. The efficiency of rotational mixing (f_c) is the main uncertain parameter for all models calculated. Its value is mainly calibrated by observations of nearby rotating stars. The choice of 0.046 was proposed by Pinsonneault et al. (1989) in order to explain solar lithium abundances, while theoretical predictions by Chaboyer & Zahn (1992) provided a somewhat different value of 0.033 which was adopted in calculations of massive rotating models done by Heger et al. (2000). A somewhat smaller value of 0.0228 calibrated against observations of massive B-type stars in the LMC was adopted by Brott et al. (2011a, 2011b).

We first computed 10 $M_{\odot}$ models for $Z = 0.0047$ (the metallicity of the LMC) for four different equatorial rotational velocities at the ZAMS: 58, 116, 232, and 345 km s^{-1} and for two cases: a case without the effects of ST on the chemical mixing included and a second case that includes those effects. Those parameters are exactly the same as those in Brott et al. (2011b). Specifically, we compare their result on the evolution of surface nitrogen enrichment presented in their Figure 8 with our results, presented in Figure 12. As can be seen, the inclusion of the ST mechanism does lead to somewhat higher surface nitrogen abundances than when it is not included, but in both cases the values we find for 12+log [N/H] are consistent with those found by Brott et al. (2011b). Interestingly, the results between the two codes agree much better when ST chemical mixing is included.

Next, we consider a 1 $M_{\odot}$ model at solar metallicity ($Z = 0.014$) for a non-rotating case and a case with a rotational velocity of 50 km s^{-1}. The effects of ST are accounted for in these models only in the transport of angular momentum and not in chemical mixing. In Figure 13 we plot the evolution of the surface helium abundance (upper left panel) as well as the evolution of the surface abundance ratios [N/C] (upper right panel) and [N/O] (lower left panel) for the non-rotating (black curve) and the rotating (red curve) case. The end of the H-burning phase is indicated with the dashed vertical line in all panels. This figure can be directly compared to the results presented in Table 2 of Ekström et al. (2012) for the same models. We see that the values for the surface He abundance we estimate with MESA at the end of the H-burning phase are generally a little higher (0.02–0.05 in mass fraction) than the ones presented by Ekström et al., but the surface abundance ratios are very similar in the two works. Any differences may be attributable to different algorithms between the codes and to numerical errors (due to differences in resolution, for example).

For another comparison of MESA including the effects of rotation and of the ST mechanism accounting only for the angular momentum transport we choose models recently presented by Yoon et al. (2012) in their investigation of the evolution of massive population III stars. Specifically, we computed a 10 $M_{\odot}$ model of zero metallicity rotating at 40% the critical rotational velocity at the ZAMS. For this model, we show the MESA-computed H-R diagram in Figure 14 that can be directly compared to the one presented by Yoon et al. (2012) in their Figure 1 (upper left panel). MESA gives similar values and ranges for the effective temperature, $T_{\rm eff}$, and the luminosity except that at later stages MESA gives slightly higher luminosities. We note that some peculiar "kinks" on the H-R track for this model are numerical artifacts related to limited resolution. Similar numerical features are also seen in calculations of rotating progenitors of GRBs by Yoon & Langer (2005; see the H-R tracks presented in their Figure 2). Also, at the end of the calculation MESA gives carbon-oxygen (C/O) core mass of 1.72 $M_{\odot}$ while Yoon et al. (2012) find it to be 1.78 $M_{\odot}$ and a surface helium mass fraction of 0.348 in contrast with 0.32 that they find.

Now we proceed to benchmark MESA against other available results that include the effects of the magnetic fields both in angular momentum transport and in mixing of chemical elements. For these comparisons we start by considering the rotating, magnetic 15 $M_{\odot}$ model at solar metallicity that was presented by Heger et al. (2005). This is the archetypical paper

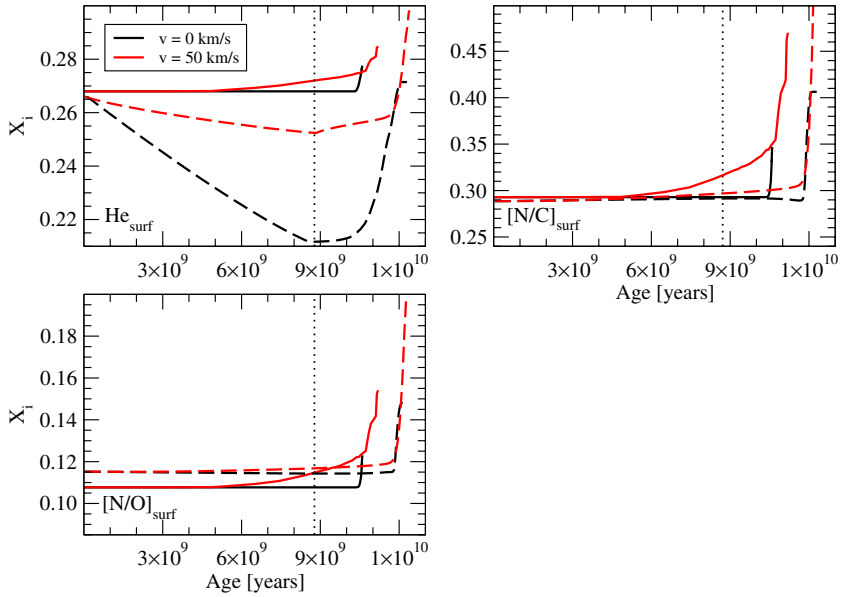

Figure 13. Evolution of the surface He abundance (upper left panel), the surface [N/C] abundance ratio (upper right panel), and the surface [N/O] abundance ratio (lower left panel) for a 1 $M_{\odot}$, $Z = 0.014$ non-rotating (black curves) model and a model with initial rotational velocity of 50 km s^{-1} (red curves) as calculated by MESA. The dotted vertical lines indicated the end of the H-burning phase for the non-rotating models. The effects of the ST mechanism on angular momentum transport were included for this model while its effects on chemical mixing are not. The dashed curves represent the results from the same models of Ekström et al. (2012).

(A color version of this figure is available in the online journal.)

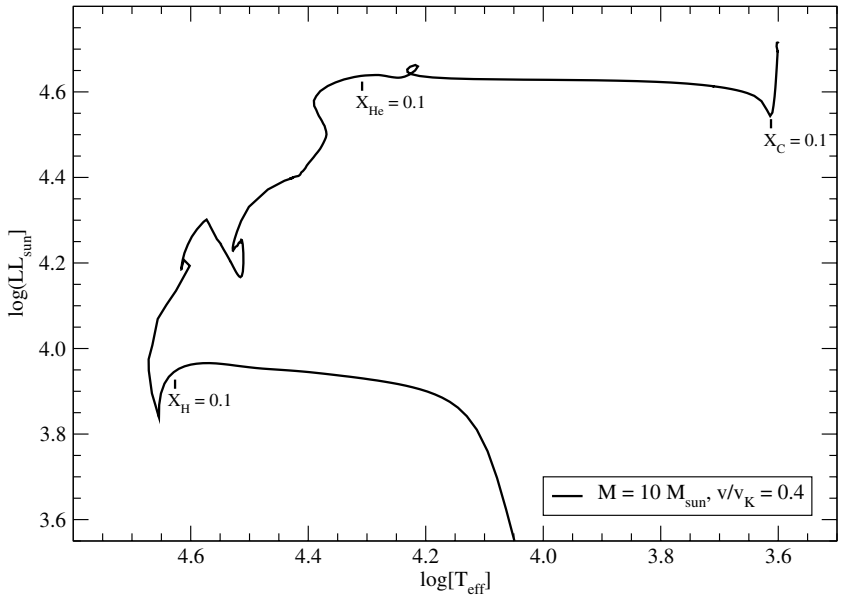

Figure 14. H-R diagram for a 10 $M_{\odot}$ zero metallicity model rotating at 40% the critical velocity at ZAMS as calculated in MESA. The effects of the ST mechanism on angular momentum transport were included for this model, but not its effects on chemical mixing. The evolutionary stages for which the central mass fractions of hydrogen, helium, and carbon are $\simeq$0.1 are indicated.

that was used to implement rotation and magnetic fields in MESA. One of the MESA built-in test problems is the same as the one we present here, and it is the original model that was used to evaluate the effects of rotation as calculated by MESA. For this model, an initial ZAMS rotational velocity of 200 km s^{-1} is used. Figure 15 shows the evolution of He, C, N, and O surface mass fractions as calculated by MESA for a non-rotating (black curves), a rotating (red curves), and a rotating plus magnetic (blue curves) case. The dashed vertical lines of the same colors represent the time at which the central hydrogen mass fraction was down to ~35% for each model in order to directly compare with the results presented in Table 6 of Heger et al. (2005). We see very good agreement of the MESA results with the results of Heger et al. (2005). We note that the inclusion of chemical mixing due to ST leads to somewhat larger abundance changes and, consequently, stronger surface nitrogen enhancements. This result is also obtained by Maeder & Meynet (2004) and they suggest that such differences might indicate that the Spruit (2002) prescriptions for chemical mixing due to magnetic fields lead to overestimates.

The other available independent calculations of stellar evolution with rotation and magnetic fields in both angular momentum

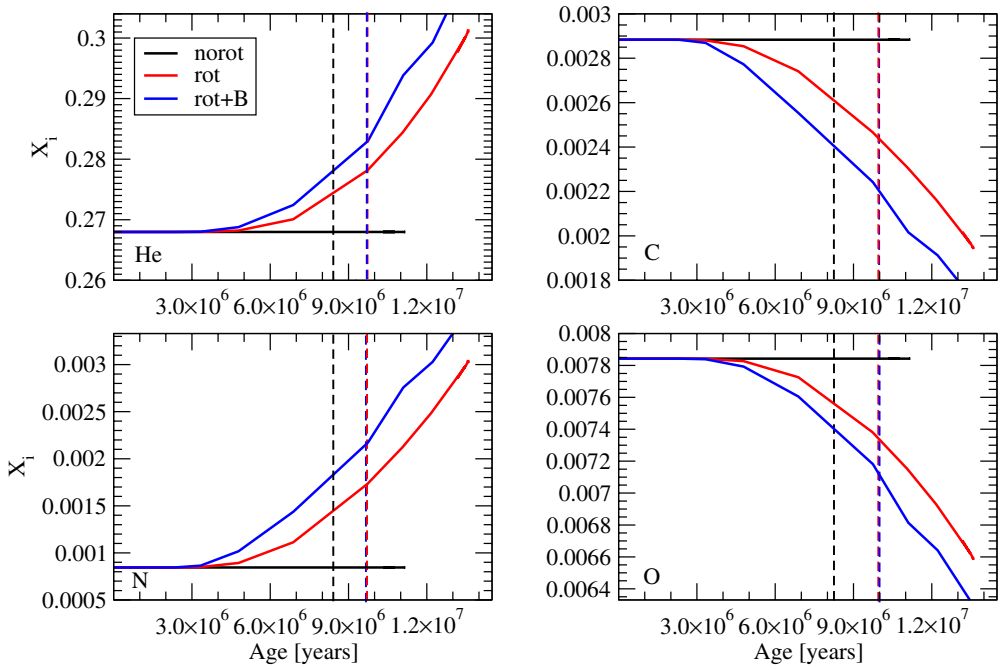

Figure 15. Evolution of the He (upper left panel), C (upper right panel), N (lower left panel), and O (lower right panel) surface mass fractions for a 15 $M_{\odot}$, $Z = 0.014$ in the case of zero rotation (black curves), initial rotation of 200 km s^{-1} (red curves), and initial rotation of 200 km s^{-1} plus magnetic fields (blue curves) as calculated in MESA. The dashed vertical lines of the same colors represent the time when the central hydrogen mass fraction was ∼35%, in accordance with Heger et al. (2005). The effects of the ST mechanism are included for both the angular momentum transport and the chemical mixing for the rotating plus magnetic models.

(A color version of this figure is available in the online journal.)

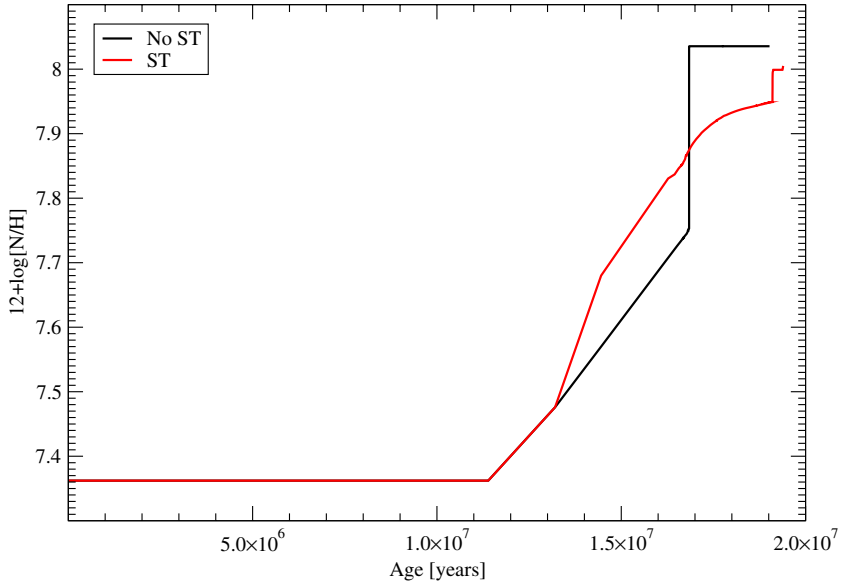

Figure 16. Evolution of surface nitrogen abundance with time for a 12 $M_{\odot}$, $Z = 0.004$ model rotating at 354.14 km s^{-1} for a case where the effects of the ST mechanism on chemical mixing are ignored (black curve) and for a case where those effects are included (red curve) as calculated by MESA. The effects of the ST mechanism on angular momentum transport were included for both models.

(A color version of this figure is available in the online journal.)

transport and chemical mixing are found in Yoon et al. (2006). To perform a comparison with MESA we select the 12 $M_{\odot}$ model with initial metallicity of $Z = 0.004$ and initial (ZAMS) equatorial rotational velocity of 354.14 km s^{-1}. In Figure 16 we show the evolution of the surface nitrogen abundance for this model as calculated by MESA in the case for which ST is not considered in chemical mixing (black curve) and in the case for which it is (red curve). At time $t = 1.93 \times 10^7$ yr, we see that 12+log [N/H] ≃ 8.1–8.4 for the two cases. Using the results presented in Table 4 of Yoon et al. (2006) we estimate that in their model 12+log [N/H] = 8.26, a value that is in good agreement with ours. At the same time in the evolution, the mass of the C/O core is 1.91 $M_{\odot}$ for the MESA model that includes the effects of ST on mixing. For the same model calculated by Yoon et al. (2006) the mass of the C/O core is 1.892 $M_{\odot}$, indicating that the mixing processes that lead to the formation of the core in the two codes also give very similar results at the same evolutionary stage.

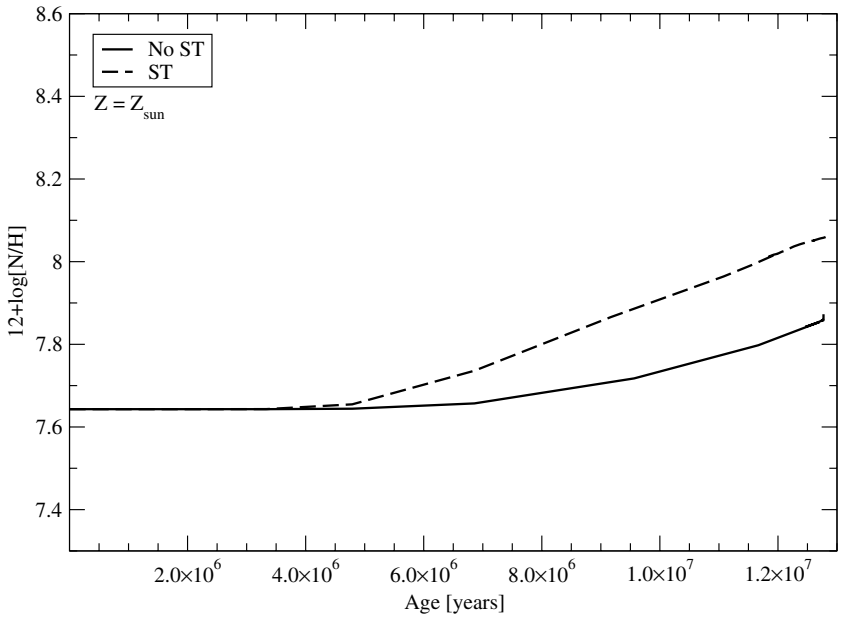

Figure 17. Evolution of 12+log [N/H] for a 15 $M_{\odot}$, $Z = 0.014$ model rotating at 150 km s^{-1} in the case where the effects of the ST mechanism on chemical mixing are ignored (solid black curve) and for a case where those effects are included (dashed black curve) as calculated by MESA. The effects of the ST mechanism on angular momentum transport were included for both models.

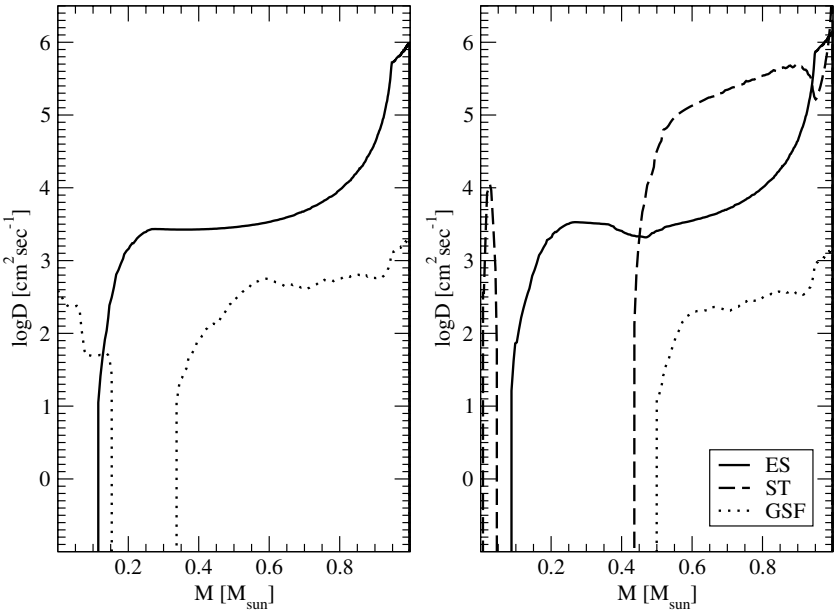

Figure 18. Distribution of the mixing coefficients due to the Eddington–Sweet circulation (ES; solid curves), the Goldreich–Schubert–Fricke instability (GSF; dotted curves), and the ST mechanism (dashed curves) for the 1 $M_{\odot}$ model rotating at 30% the critical value in a case where ST mixing is ignored (left panel) and in a case where it is included (right panel). The effects of the ST mechanism on angular momentum transport were included in all cases.

The comparison of MESA stellar evolution with rotation and magnetic fields to these other codes indicates that MESA accounts for these effects as well as they do, specifically if one accounts for differences between codes, numerical errors, different model resolutions, and specific numerical techniques that can interact in nonlinear ways. Major indicators of the effects of rotation and magnetic fields on chemical mixing such as surface nitrogen and helium enrichments and C/O core masses are found to have a similar range of values amongst different stellar evolution codes.

This agreement enables us to take a step further and directly compare the MESA results on surface nitrogen abundances of rotating stars with spectroscopic observations of rotating stars in the Milky Way, the LMC, and the SMC recently presented by the VLT-FLAMES survey of massive stars (Hunter et al. 2008, 2009). To enable this comparison, we computed an additional MESA model for a 15 $M_{\odot}$ star at solar metallicity ($Z = 0.014$) rotating at 150 km s^{-1} for two cases: one with the effects of the ST mechanism on chemical mixing ignored and one with those effects considered. The evolution of 12+log [N/H] for this model is presented in Figure 17. Direct comparison with Figure 6 of Hunter et al. (2009) illustrates that MESA estimates for the range of 12+log [N/H] values are consistent with those measured for massive rotating stars in the Milky Way. Similar results are obtained for the same model at the higher rotational velocity of 200 km s^{-1}, which we calculated in order to compare

with the results of Heger et al. (2005). The higher rotational velocity led to slightly higher values for 12+log [N/H] but still within the range of the observations presented by Hunter et al. (2009). In addition, the models that we calculated for a metallicity of $Z = 0.0047$ in order to compare with the results of Brott et al. (2011b) show 12+log [N/H] values (Figure 12) that agree very well with the observations of Hunter et al. (2009) for massive early B-type stars in the LMC (their Figure 5).

As we mentioned above, there are currently no existing 12+log [N/H] observations in single solar-type rapidly rotating stars that can be compared to evolutionary model predictions in the low-mass range. Just such a comparison was the initial observational motivation of the present work: to account for carbon depletion in the secondary stars of some CVs and LMXBs which are close binaries and tidally locked, therefore rapidly rotating, based on calibrations that have been done for higher-mass stars (and for the Sun) for which observations are available. There certainly is a degree of uncertainty associated with the calculations, specifically when the effects of the ST mechanism on chemical mixing are included. In general, the inclusion of these effects leads to somewhat higher abundances for some models of massive rapidly rotating stars than those suggested by some observations while in some calculations the results are consistent with observations (Maeder & Meynet 2005). Given the differences in computational algorithm that were discussed above and the uncertainties in the measurement of initial metallicities (upon which the results for surface abundance changes are sensitive) it remains unclear whether the inclusion of the effects of ST mixing necessarily leads to wrong results. In the cases investigated by this paper it is suggested that those effects of increased mixing efficiency due to the ST mechanism are necessary if rotation and magnetic fields can be used as an explanation. To illustrate the importance of ST mixing in our models we present the distribution of the diffusion coefficients due to meridional circulation (ES circulation), the GSF, and the ST mechanism in Figure 18 for one of our models (1 $M_{\odot}$ rotating at 30% the critical value) at about the half of its MS lifetime for a case where ST was ignored in calculations of the chemical mixing (left panel) and a case where ST was included (right panel). From this plot it is obvious that ST dominates chemical mixing through most of the stellar interior as well as the surface, and in some cases it is more than an order of magnitude more important than meridional circulation.

REFERENCES

Andronov, N., Pinsonneault, M., & Sills, A. 2003, ApJ, 582, 358
Ashok, N. M., & Banerjee, D. P. K. 2003, A&A, 409, 1007
Asplund, M., Grevesse, N., & Sauval, A. J. 2005, in ASP Conf. Ser. 336, Cosmic Abundances as Records of Stellar Evolution and Nucleosynthesis, ed. T. G. Barnes, III & F. N. Bash (San Francisco, CA: ASP), 25
Belczynski, K., Kalogera, V., Rasio, F. A., et al. 2008, ApJS, 174, 223
Bitner, M. A., Robinson, E. L., & Behr, B. B. 2007, ApJ, 662, 564
Bloemen, S., Marsh, T. R., Degroote, P., et al. 2012, MNRAS, 422, 2600
Breton, R. P., Rappaport, S. A., van Kerkwijk, M. H., & Carter, J. A. 2012, ApJ, 748, 115
Brott, I., de Mink, S. E., Cantiello, M., et al. 2011a, A&A, 530, A115
Brott, I., Evans, C. J., Hunter, I., et al. 2011b, A&A, 530, A116
Brott, I., Hunter, I., de Koter, A., et al. 2009, Commun. Asteroseismol., 158, 55
Brown, B. P., Miesch, M. S., Browning, M. K., Brun, A. S., & Toomre, J. 2011, ApJ, 731, 69
Carter, J. A., Rappaport, S., & Fabrycky, D. 2011, ApJ, 728, 139
Cassisi, S., Iben, I., Jr., & Tornambe, A. 1998, ApJ, 496, 376
Chaboyer, B., & Zahn, J.-P. 1992, A&A, 253, 173
Chatzopoulos, E., & Wheeler, J. C. 2012, ApJ, 748, 42
Davies, M. B., Piotto, G., & de Angeli, F. 2004, MNRAS, 349, 129
de Jager, C., Nieuwenhuijzen, H., & van der Hucht, K. A. 1988, A&AS, 72, 259
de Mink, S. E., Cantiello, M., Langer, N., et al. 2009, A&A, 497, 243
Eggenberger, P., Meynet, G., Maeder, A., et al. 2008, Ap&SS, 316, 43
Ekström, S., Georgy, C., Eggenberger, P., et al. 2012, A&A, 537, A146
Ekström, S., Meynet, G., Chiappini, C., Hirschi, R., & Maeder, A. 2008, A&A, 489, 685
Eracleous, M., Horne, K., Robinson, E. L., et al. 1994, ApJ, 433, 313
Ergma, E., & Antipova, J. 1999, A&A, 343, L45
Ferraro, F. R., Beccari, G., Dalessandro, E., et al. 2009, Nature, 462, 1028
Ferraro, F. R., Sabbi, E., Gratton, R., et al. 2006, ApJ, 647, L53
Ferraro, F. R., Sills, A., Rood, R. T., Paltrinieri, B., & Buonanno, R. 2003, ApJ, 588, 464
Froning, C. S., Cantrell, A. G., Maccarone, T. J., et al. 2011, ApJ, 743, 26
Froning, C. S., Robinson, E. L., & Bitner, M. A. 2007, ApJ, 663, 1215
Fusi Pecci, F., Ferraro, F. R., Corsi, C. E., Cacciari, C., & Buonanno, R. 1992, AJ, 104, 1831
Gänsicke, B. T., Szkody, P., de Martino, D., et al. 2003, ApJ, 594, 443
Gelino, D. M., Balman, Ş, Kızıloğlu, Ü., et al. 2006, ApJ, 642, 438
Glebbeek, E., Gaburov, E., de Mink, S. E., Pols, O. R., & Portegies Zwart, S. F. 2009, A&A, 497, 255
Goranskij, V., Shugarov, S., Zharova, A., Kroll, P., & Barsukova, E. A. 2010, Perem. Zvezdy, 30, 4
Hanes, D. A. 1985, MNRAS, 213, 443
Han, Z., & Podsiadlowski, P. 2004, MNRAS, 350, 1301
Harrison, T. E., Osborne, H. L., & Howell, S. B. 2004, AJ, 127, 3493
Harrison, T. E., Osborne, H. L., & Howell, S. B. 2005, AJ, 129, 2400
Haswell, C. A., Hynes, R. I., King, A. R., & Schenker, K. 2002, MNRAS, 332, 928
Heger, A., Langer, N., & Woosley, S. E. 2000, ApJ, 528, 368
Heger, A., Woosley, S. E., & Spruit, H. C. 2005, ApJ, 626, 350
Hills, J. G., & Day, C. A. 1976, Astrophys. Lett., 17, 87
Hunter, I., Brott, I., Langer, N., et al. 2009, A&A, 496, 841
Hunter, I., Brott, I., Lennon, D. J., et al. 2008, ApJ, 676, L29
IbanoğLu, C., DervişoğLu, A., Ćakırlı, Ö., Sipahi, E., & Yüce, K. 2012, MNRAS, 419, 1472
Iben, I., Jr., & Tutukov, A. V. 1989, ApJ, 342, 430
Iben, I., Jr., & Tutukov, A. V. 1994, ApJ, 431, 264
Ivanova, N., & Taam, R. E. 2003, ApJ, 599, 516
Jameson, R. F., King, A. R., & Sherrington, M. R. 1980, MNRAS, 191, 559
Kasliwal, M. M., Kulkarni, S. R., Gal-Yam, A., et al. 2010, ApJ, 723, L98
Kato, M., & Hachisu, I. 1999, ApJ, 513, L41
Kato, M., & Hachisu, I. 2003, ApJ, 598, L107
Kato, M., Hachisu, I., Kiyota, S., & Saio, H. 2008, ApJ, 684, 1366
Krishnamurthi, A., Pinsonneault, M. H., Barnes, S., & Sofia, S. 1997, ApJ, 480, 303
Langer, N., Yoon, S.-C., Wellstein, S., & Scheithauer, S. 2002, in ASP Conf. Ser. 261, The Physics of Cataclysmic Variables and Related Objects, ed. B. T. Gänsicke, K. Beuermann, & K. Reinsch (San Francisco, CA: ASP), 252
Lipunov, V. M., Postnov, K. A., Prokhorov, M. E., & Bogomazov, A. I. 2009, Astron. Rep., 53, 915
Livio, M., & Truran, J. W. 1992, ApJ, 389, 695
Lovisi, L., Mucciarelli, A., Ferraro, F. R., et al. 2010, ApJ, 719, L121
Maeder, A. 1987, A&A, 173, 247
Maeder, A., & Meynet, G. 2003, A&A, 411, 543
Maeder, A., & Meynet, G. 2004, A&A, 422, 225
Maeder, A., & Meynet, G. 2005, A&A, 440, 1041
Maeder, A., & Meynet, G. 2011, arXiv:1109.6171
Mathieu, R. D., & Geller, A. M. 2009, Nature, 462, 1032
Maxted, P. F. L., Marsh, T. R., & North, R. C. 2000, MNRAS, 317, L41
McCrea, W. H. 1964, MNRAS, 128, 147
Meng, X., & Yang, W. 2010, ApJ, 710, 1310
Mereghetti, S., La Palombara, N., Tiengo, A., et al. 2011, ApJ, 737, 51
Neugent, K. F., Massey, P., Skiff, B., & Meynet, G. 2012, ApJ, 749, 177
O'Brien, M. S., Bond, H. E., & Sion, E. M. 2001, ApJ, 563, 971
Paczyński, B. 1967, Acta Astron., 17, 287
Paczyński, B. 1971, ARA&A, 9, 183
Paczynski, B., & Sienkiewicz, R. 1981, ApJ, 248, L27
Paxton, B., Bildsten, L., Dotter, A., et al. 2011, ApJS, 192, 3
Pinsonneault, M. H., Kawaler, S. D., Sofia, S., & Demarque, P. 1989, ApJ, 338, 424
Podsiadlowski, P., Han, Z., & Rappaport, S. 2003, MNRAS, 340, 1214
Podsiadlowski, P., Rappaport, S., & Pfahl, E. D. 2002, ApJ, 565, 1107
Poznanski, D., Chornock, R., Nugent, P. E., et al. 2010, Science, 327, 58
Rappaport, S., Verbunt, F., & Joss, P. C. 1983, ApJ, 275, 713
Rogers, F. J., & Nayfonov, A. 2002, ApJ, 576, 1064
Ruiter, A. J., Belczynski, K., & Fryer, C. 2009, ApJ, 699, 2026
Ruiter, A. J., Belczynski, K., Sim, S. A., et al. 2011, MNRAS, 417, 408
Saio, H., & Wheeler, J. C. 1980, ApJ, 242, 1176

Sandage, A. R. 1953, AJ, 58, 61
Schaefer, B. E., & Pagnotta, A. 2012, Nature, 481, 1
Schenker, K., King, A. R., Kolb, U., Wynn, G. A., & Zhang, Z. 2002, MNRAS, 337, 1105
Sekiguchi, K., Caldwell, J. A. R., Stobie, R. S., & Buckley, D. A. H. 1990, MNRAS, 245, 28P
Sekiguchi, K., Catchpole, R. M., Fairall, A. P., et al. 1989, MNRAS, 236, 61
Shen, K. J., Kasen, D., Weinberg, N. N., Bildsten, L., & Scannapieco, E. 2010, ApJ, 715, 767
Shore, S. N., Sonneborn, G., Starrfield, S. G., et al. 1991, ApJ, 370, 193
Sills, A., Pinsonneault, M. H., & Terndrup, D. M. 2000, ApJ, 534, 335
Sion, E. M., Godon, P., Myzcka, J., & Blair, W. P. 2010, ApJ, 716, L157
Solheim, J.-E., & Yungelson, L. R. 2005, in ASP Conf. Ser. 334, 14th European Workshop on White Dwarfs, ed. D. Koester & S. Moehler (San Francisco, CA: ASP), 387
Spruit, H. C. 1999, A&A, 349, 189
Spruit, H. C. 2002, A&A, 381, 923
Spruit, H. C. 2006, arXiv:astro-ph/0607164
Starrfield, S., Sonneborn, G., Sparks, W. M., et al. 1988, in A Decade of UV Astronomy with the IUE Satellite (ESA SP-281; Noordwijk: ESA), 167
Tanaka, Y., & Lewin, W. H. G. 1995, in X-ray Binaries, ed. W. H. G. Lewin, J. van Paradijs, & E. P. J. van den Heuvel (Cambridge: Cambridge Univ. Press), 126
Timmes, F. X. 1999, ApJS, 124, 241
Timmes, F. X., & Swesty, F. D. 2000, ApJS, 126, 501
Truran, J. W., Livio, M., Hayes, J., Starrfield, S., & Sparks, W. M. 1988, ApJ, 324, 345
Warner, B. (ed.) 2003, Cataclysmic Variable Stars (Cambridge: Cambridge Univ. Press)
Wheeler, J. C. 1979, ApJ, 234, 569
Willems, B., & Kolb, U. 2004, A&A, 419, 10
van der Sluys, M. V., Verbunt, F., & Pols, O. R. 2005, A&A, 440, 973
van Kerkwijk, M. H., Rappaport, S. A., Breton, R. P., et al. 2010, ApJ, 715, 51
Verbunt, F., & Zwaan, C. 1981, A&A, 100, L7
Wang, B., Meng, X., Chen, X., & Han, Z. 2009a, MNRAS, 395, 847
Wang, B., Chen, X., Meng, X., & Han, Z. 2009b, ApJ, 701, 1540
Wang, B., & Han, Z. 2009, A&A, 508, L27
Weaver, T. A., Zimmerman, G. B., & Woosley, S. E. 1978, ApJ, 225, 1021
Webbink, R. F., Livio, M., Truran, J. W., & Orio, M. 1987, ApJ, 314, 653
Willems, B., Kolb, U., Sandquist, E. L., Taam, R. E., & Dubus, G. 2005, ApJ, 635, 1263
Williams, R. E., Sparks, W. M., Gallagher, J. S., et al. 1981, ApJ, 251, 221
Woudt, P. A., Steeghs, D., Karovska, M., et al. 2009, ApJ, 706, 738
Yoon, S.-C., Dierks, A., & Langer, N. 2012, arXiv:1201.2364
Yoon, S.-C., & Langer, N. 2003, A&A, 412, L53
Yoon, S.-C., & Langer, N. 2005, A&A, 443, 643
Yoon, S.-C., Langer, N., & Norman, C. 2006, A&A, 460, 199
Zahn, J.-P. 1975, A&A, 41, 329
Zahn, J.-P. 1977, A&A, 57, 383
Zahn, J.-P. 1989, A&A, 220, 112